Nonlinear Vibration of a Multi-Degree-of-Freedom Gear Transmission System With Multipiecewise Linear Functions

F. L. Liao
Department of Applied Mechanics and Engineering,
Sun Yat-sen University,
Guangzhou 510275, China

J. L. Huang[1]
Department of Applied Mechanics and Engineering,
Sun Yat-sen University,
Guangzhou 510275, China
e-mail: huangjl@mail.sysu.edu.cn

W. D. Zhu
Department of Mechanical Engineering,
University of Maryland, Baltimore County,
1000 Hilltop Circle,
Baltimore, MD 21250
e-mail: wzhu@umbc.edu

Periodic and period-doubling vibrations in a gear transmission system subjected to forced excitations with multipiecewise linear functions are investigated in this work by using the incremental harmonic balance (IHB) method. The nonlinear ordinary differential equations that govern vibration of the gear transmission system are formulated by employing the Newton's second law. Analytical results reveal abundant interesting phenomena, including jumps, bifurcations, softening-spring behaviors, and primary, superharmonic, and subharmonic resonances, which have not been exhibited in existing investigations on nonlinear vibrations of gear transmission systems. Nonlinear phenomena and resonances of the gear transmission system are revealed by considering different numbers of degrees-of-freedom of the system. The bifurcations containing saddle-node, period-doubling, and Hopf bifurcations are observed in frequency response curves. The period-doubling phenomena are characterized by phase-plane diagrams and Fourier spectra. Further, analytical results obtained by the IHB method match very well with those from numerical integration. [DOI: 10.1115/1.4056850]

Keywords: gear transmission system, multipiecewise linear functions, nonlinear vibration, incremental harmonic balance method, bifurcation

1 Introduction

Gear transmission systems can be found in a wide range of industrial applications, such as wind turbines, ship rolls, swings, automobiles, aircraft, and other machinery transmission systems. Analytical models of gear transmission systems have been extensively studied in the last few decades. The vast literature on nonlinear vibrations of gear transmission systems has been reviewed by Wang et al. [1] up to 2003. Problems of gear transmission systems have been tackled in analysis of particular aspects such as dynamic models, analysis methods, and nonlinear phenomena. Most of those studies addressed problems of backlashes, time-varying mesh stiffnesses of teeth, gear transmission errors, and time-varying support stiffnesses of geared systems [2,3].

Dynamic models of gear transmission systems are constantly investigated in order to develop more suitable models to reveal nonlinear phenomena concealed in them over the past decades. Sheng et al. [4] developed a new nonlinear gear dynamic model that introduced both tribological and dynamic characteristics of gears during meshing. Li et al. [5] established a multi-degree-of-freedom (DOF) gear dynamic model that considered nonlinear factors of gear meshing such as time-varying mesh stiffnesses and gear backlashes for the sake of analyzing effects of tooth tribologies on gear dynamic responses. Li et al. [6] proposed a coupled tribodynamic model of a spur gear pair; this dynamic model introduced both a load-dependent combined mesh stiffness and nonlinear backlash caused by the lubricant between teeth, and numerical simulation results of their investigation indicated that there was an obvious reduction in the vibration amplitude under the effect of the lubricant compared with the traditional model that ignored the lubrication effect. Li and Kahraman [7] investigated a tribodynamic model that included a mixed elastohydrodynamic lubrication characteristic and transverse-torsional vibration of a spur gear transmission system and introduced constant damping, time-varying mesh stiffness, backlash expressed in the form of a piecewise linear function, and transmission error. As reviewed by some researchers, besides the models that considered tribodynamic characteristics, a great number of published bibliographies proposed other reliable nonlinear dynamic models for gear systems, where friction between meshing teeth was neglected. Jiang et al. [8] proposed a dynamic model of a coal cutter gear system, which considered multifrequency excitation and a backlash function fitted by a cubic polynomial function. Chen et al. [9] presented an improved spur gear dynamic model that introduced tooth stiffness, fillet-foundation stiffness, bending stiffness, shear stiffness, axial comprehensive stiffness, tooth contact stiffness caused by detailed deformations of individual teeth, and additional stiffness, and demonstrated the reliability of this dynamic model employing experimental data. Litak et al. [10] discussed a dynamic model of a single-DOF gear transmission system, which included mesh stiffness characterized by a periodically changing function and backlash described by a piecewise linear function, and took effects of tooth shape imperfections and defects into account. According to differences in methods for modeling, investigators developed some innovative dynamic models that were different from the above-mentioned lumped-mass models. Parker et al. [11] investigated a contact mechanics model of a spur gear pair by the finite element method and validated it by employing experiments. Dong et al. [12] treated a gear pair as Timoshenko beam elements and proposed a dynamic model with the finite element theory. A comparison between theoretical data and experimental results showed that Timoshenko beam elements were effective and reliable to represent the dynamic response of a gear system. Further, according to the way of characterizing a piecewise linear function contained in a gear transmission system, some researchers developed interesting dynamic models, where the piecewise linear function was fitted by a polynomial. Theodossiades and Natsiavas [13] developed an approximate model of a gear pair, in which the piecewise linear function was approximately described by a cubic polynomial, and numerical results from their paper indicated that

[1]Corresponding author.

Manuscript received October 3, 2022; final manuscript received February 1, 2023; published online March 2, 2023. Assoc. Editor: Zaihua Wang.

the model with the cubic polynomial presented inaccurate results compared with that considering the piecewise linear function.

Nonlinear vibrations of gear transmission systems are of great importance and interesting phenomena can be explored in piecewise linear systems with multiple DOFs. Dynamic analysis of a gear system under internal and external excitations has been intensively discussed in the literature. Moradi and Salarieh [14] investigated the dynamic response of a gear system employing the multiple-scale method and defined a detuning parameter to describe the deviation between the engine excitation frequency and a natural frequency of the gear system. Results indicated that frequency response curves presented stable and unstable areas and jump phenomena; besides, under an excitation torque, the system showed other interesting nonlinear behaviors, such as superharmonic and subharmonic resonances. Guo and Parker [15] explored the periodic response of a planetary gear system by utilizing the harmonic balance method with arc-length continuation. Their investigation exhibited abundant nonlinear characteristics that included a jump phenomenon due to saddle-node bifurcation, a softening-spring behavior caused by tooth separation, and a hardening-spring behavior induced by transition from no-bearing contact to contact, and discovered secondary Hopf and period-doubling bifurcations that were the routes to chaos. Kahraman and Singh [16] examined the frequency response behavior of a gear rotor-bearing system considering a time-varying mesh stiffness by utilizing the multiple-scale method. Their investigation revealed some nonlinear phenomena that included superharmonic and subharmonic resonances, a jump from a stable state to another stable state via saddle-node bifurcation, and a softening-spring nonlinear behavior. Besides the above-mentioned analytical methods, some investigators employed numerical integration to reveal nonlinear dynamic behaviors of gear transmission systems. Cao et al. [17] predicted the dynamic response of a gear transmission system, which included a jump phenomenon, a weak softening-spring nonlinearity, and super-harmonic resonance, by adopting the fourth-order Runge–Kutta (RK) method. Guilbault et al. [18] investigated the three-dimensional nonlinear vibration of a cylindrical gear system by applying the fourth-order RK method. Their research revealed primary resonance, subharmonic resonance, and a softening-spring nonlinear behavior of the system. Nonlinear vibrations of gear transmission systems have been investigated by many researchers in the past. Recent studies in nonlinear vibrations of gear transmission systems show that the problems are still of interest to researchers. Mo et al. [19] investigated the nonlinear vibration of a nonorthogonal face gear-rotor-bearing system by employing the multiple-scale method, and they analyzed primary resonance characteristics of the system and determined its stability. Sun et al. [20] analyzed the vibration response of a gear-rotor-bearing system by considering influences of thermal expansion and temperature on material behaviors. They indicated that the system got into chaotic motion from periodic motion with a temperature increase in part of its speed range. Wang and Zhu [21] discussed the nonlinear dynamics of a fixed-axis spur planetary gear-rotor-bearing system by using the fourth-order RK method. They identified diverse nonlinear behaviors of the system through global bifurcations. Lin et al. [22] examined the dynamic response of an eccentric curve-face gear transmission model that considered effects of gear eccentricity, the time-varying helical angle, and the input velocity by employing the fourth-order RK method. They concluded that gear eccentricity can regulate the amplitude and frequency of the response. Zhang et al. [23] identified nonlinear dynamic characteristics of a wind turbine compound gear transmission system by using the fourth-order RK method. Their investigation discussed complex nonlinear behaviors of the system including periodic, quasi-periodic, and chaotic responses.

The incremental harmonic balance (IHB) method was first presented by Lau and Cheung [24–26], and it was later developed to investigate dynamic responses of one-DOF systems with piecewise linearities [27]. Shen et al. [28] used the IHB method to examine the dynamic response of a one-DOF gear transmission system with piecewise linearity. The IHB method is extended in the current work to determine periodic and period-doubling responses of a gear transmission system with three DOFs with multipiecewise linear functions. According to characteristics of piecewise linear functions, an improved Floquet theory is formulated in order to analyze stability of periodic and period-doubling responses. Further, bifurcation types of responses of the system are determined by Floquet multipliers. Finally, nonlinear phenomena including jumps, softening-spring behaviors, and resonances containing primary, superharmonic, and subharmonic resonances are discussed.

The main objective of this work is to reveal nonlinear dynamic responses of gear transmission systems with multipiecewise linear functions, and various responses under internal and external excitations. The rest of this work is organized as follows. The multi-DOF dynamic model of a gear transmission system under internal and external excitations is proposed in Sec. 2 utilizing the lumped-mass method to simplify the gear transmission system. The governing equation of the gear transmission system is developed by employing the Newton's second law. The IHB method is formulated in Sec. 3 to calculate periodic and period-doubling responses of the multidimensional dynamic model of the gear transmission system with three piecewise linear functions due to backlashes and bearing clearances. Stability of the periodic and period-doubling responses and types of various bifurcation points are examined in Sec. 4 by employing the Floquet theory. In Sec. 5, nonlinear dynamic phenomena including the jump phenomenon, primary, superharmonic, and subharmonic resonances due to internal and external excitations, and bifurcation types of responses of the system are discussed, and various dynamic responses under internal and external excitations are analyzed. Finally, the main conclusions of this work are presented in Sec. 6.

2 Gear Transmission System With Multipiecewise Linear Functions

During the operation of a gear transmission system, multiple directional vibrations can occur including radial vibration caused by rolling element bearings, torsional vibration between teeth, and axial motion parallel to flexible shafts supported by rolling element bearings [29]. In this work, a dynamic model of a gear transmission system is illustrated in Fig. 1. By considering radial and torsional vibrations, the dynamic model composed of a spur gear pair mounted on shafts and two pairs of rolling element bearings fixed on the gearbox is proposed by employing the lumped-mass method [30]. In order to simplify the nonlinear dynamic model, the following assumptions are made. The gearbox is assumed to

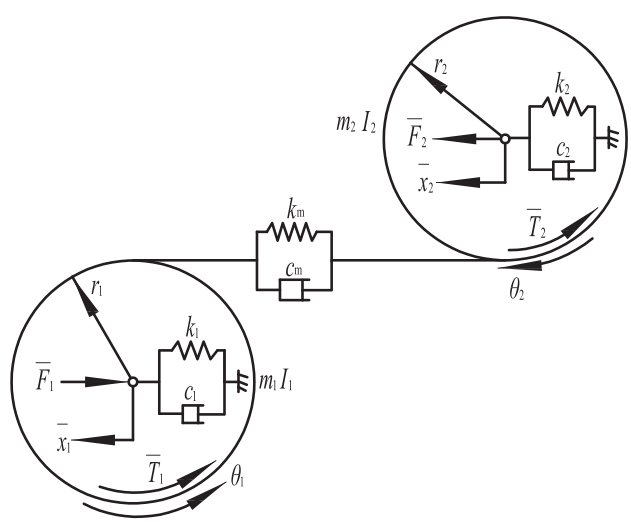

Fig. 1 Multi-DOF dynamic model of a gear transmission system

be rigid; the effect of the prime mover or load inertia on the system is not included, and the axial motion is neglected. As shown in Fig. 1, two rigid disks are connected by a spring and damper acting on the line of action that is normal to the tooth flank; m_1, m_2, r_1, r_2, I_1, and I_2 denote gear masses, base circle radii, and mass moments of inertia of the driving gear and driven gear, respectively. The gear mesh acting on the line of action between teeth is represented by the mesh stiffness k_m and mesh damping c_m, and the friction force at the mesh point is not taken into account. Therefore, the transverse vibration along the pressure line direction is not coupled with the motion that is perpendicular to the pressure line. The flexible shafts and bearings supporting the ith gear are modeled by k_i and c_i that represent the supporting stiffnesses and damping, respectively. High-frequency internal excitation provided by the static transmission error and low-frequency external excitation caused by input torque fluctuations are included in the nonlinear dynamic model of the gear transmission system with multipiecewise linear functions. The time-varying input torque is $\bar{T}_1(\bar{t}) = \bar{T}_{1m} + \bar{T}_{1a}(\bar{t})$, where $\bar{T}_{1m}$ and $\bar{T}_{1a}(\bar{t})$ are the average component and time-varying component of the input torque, respectively. The output torque is deemed to be invariant, i.e., $\bar{T}_2(\bar{t}) = \bar{T}_{2m}$; $\bar{F}_1$ and $\bar{F}_2$ are external radial loads that are applied to all the rolling element bearings [30].

Governing equations of the gear transmission system with multipiecewise linear functions can be formulated by employing the Newton's second law and defining $\bar{x}_m = \bar{x}_1 - \bar{x}_2 - \bar{e}$ and $\bar{x}(\bar{t}) = r_1\theta_1(\bar{t}) - r_2\theta_2(\bar{t})$:

$$m_1\ddot{\bar{x}}_1 + c_1\dot{\bar{x}}_1 + c_m(\dot{\bar{x}} + \dot{\bar{x}}_m) + k_1 f_1(\bar{x}_1) + k_m f_m(\bar{x} + \bar{x}_m) = -\bar{F}_1 \tag{1}$$

$$m_2\ddot{\bar{x}}_2 + c_2\dot{\bar{x}}_2 - c_m(\dot{\bar{x}} + \dot{\bar{x}}_m) + k_2 f_2(\bar{x}_2) - k_m f_m(\bar{x} + \bar{x}_m) = \bar{F}_2 \tag{2}$$

$$I_1\ddot{\theta}_1 + c_m r_1(\dot{\bar{x}} + \dot{\bar{x}}_m) + r_1 k_m f_m(\bar{x} + \bar{x}_m) = \bar{T}_1 \tag{3}$$

$$I_2\ddot{\theta}_2 - c_m r_2(\dot{\bar{x}} + \dot{\bar{x}}_m) - r_2 k_m f_m(\bar{x} + \bar{x}_m) = -\bar{T}_2 \tag{4}$$

where $\dot{}$ and $\ddot{}$ denote the first and second derivatives with respect to time $\bar{t}$, respectively; $\bar{x}_i$ and θ_i $(i = 1, 2)$ are the radial displacement and the angular displacement of the ith gear, respectively; $f_1(\cdot)$ and $f_2(\cdot)$ are piecewise linear displacements in the radial direction of the driving gear and driven gear, respectively; $f_m(\cdot)$ is the piecewise linear displacement related to the gear mesh; and $\bar{e}(\bar{t})$ is the static transmission error with $\bar{e}(\bar{t}) = \tilde{e}\sin(\bar{\Omega}_m\bar{t} + \phi_m)$, in which $\tilde{e}$ is the excitation amplitude, $\bar{\Omega}_m$ is the excitation frequency, and ϕ_m is the phase angle of internal excitation due to gear backlashes and radial clearances in rolling element bearings.

Let

$$m_c = 1\Big/\left(\frac{r_1^2}{I_1} + \frac{r_2^2}{I_2}\right) \tag{5}$$

where m_c is the equivalent mass representing the total inertial of the gear pair. Substituting Eq. (5) into Eqs. (3) and (4) yields

$$m_c\ddot{\bar{x}} + c_m(\dot{\bar{x}} + \dot{\bar{x}}_m) + k_m f_m(\bar{x} + \bar{x}_m) = \bar{F}_3 + \bar{F}_{aT}(\bar{t}) \tag{6}$$

where $\bar{F}_3 = \bar{T}_{1m}/r_1 = \bar{T}_{2m}/r_2$ is the average force transmitted by the gear pair, and $\bar{F}_{aT}(\bar{t}) = m_c\bar{T}_{1a}(\bar{t})/2I_1$ is a fluctuating force due to the external input torque.

Introducing a new variable $\bar{x}_3(\bar{t})$ that denotes the difference between the dynamic transmission error and static transmission error $\bar{e}(\bar{t})$:

$$\bar{x}_3(\bar{t}) = \bar{x}(\bar{t}) + \bar{x}_m(\bar{t}) \tag{7}$$

and substituting Eq. (7) into Eqs. (1), (2), and (6) yields

$$\begin{bmatrix} m_1 & 0 & 0 \\ 0 & m_2 & 0 \\ -m_c & m_c & m_c \end{bmatrix}\begin{Bmatrix} \ddot{\bar{x}}_1(\bar{t}) \\ \ddot{\bar{x}}_2(\bar{t}) \\ \ddot{\bar{x}}_3(\bar{t}) \end{Bmatrix} + \begin{bmatrix} c_1 & 0 & c_m \\ 0 & c_2 & -c_m \\ 0 & 0 & c_m \end{bmatrix}\begin{Bmatrix} \dot{\bar{x}}_1(\bar{t}) \\ \dot{\bar{x}}_2(\bar{t}) \\ \dot{\bar{x}}_3(\bar{t}) \end{Bmatrix} + \begin{bmatrix} k_1 & 0 & k_m \\ 0 & k_2 & -k_m \\ 0 & 0 & k_m \end{bmatrix}\begin{Bmatrix} f_1(\bar{x}_1) \\ f_2(\bar{x}_2) \\ f_m(\bar{x}_3) \end{Bmatrix} = \begin{Bmatrix} -\bar{F}_1 \\ \bar{F}_2 \\ \bar{F}_3 - m_c\ddot{\bar{e}}(\bar{t}) + \bar{F}_{aT}(\bar{t}) \end{Bmatrix} \tag{8}$$

For simplicity, the following dimensionless variables are introduced: $x_i(\bar{t}) = \bar{x}_i(\bar{t})/b\ (i = 1, 2, 3)$, $\omega_n = \sqrt{k_m/m_c}$, $\omega_i = \sqrt{k_i/m_i}$ $(i = 1, 2)$, and $t = \omega_n\bar{t}$, where b is the characteristic length. Here the fluctuating force $\bar{F}_{aT}(\bar{t})$ is expressed in the form of a harmonic function $\bar{F}_{aT} = \tilde{F}_{aT}\sin(\bar{\Omega}_T\bar{t} + \phi_T)$, where $\tilde{F}_{aT}$ is the excitation amplitude, $\bar{\Omega}_T$ is the excitation frequency, and ϕ_T is the phase angle of external excitation caused by torque fluctuations. Further, by letting $\Omega_m = \bar{\Omega}_m/\omega_n$ and $\Omega_T = \bar{\Omega}_T/\omega_n$, dimensionless excitation frequencies are obtained in order to yield the following dimensionless governing equations of the system:

$$\begin{bmatrix} 1 & 0 & 0 \\ 0 & 1 & 0 \\ -1 & 1 & 1 \end{bmatrix}\begin{Bmatrix} x_1(t) \\ x_2(t) \\ x_3(t) \end{Bmatrix} + 2\begin{bmatrix} \zeta_{11} & 0 & \zeta_{13} \\ 0 & \zeta_{22} & -\zeta_{23} \\ 0 & 0 & \zeta_{33} \end{bmatrix}\begin{Bmatrix} \dot{x}_1(t) \\ \dot{x}_2(t) \\ \dot{x}_3(t) \end{Bmatrix} + \begin{bmatrix} k_{11} & 0 & k_{13} \\ 0 & k_{22} & -k_{23} \\ 0 & 0 & 1 \end{bmatrix}\begin{Bmatrix} f_1(x_1) \\ f_2(x_2) \\ f_m(x_3) \end{Bmatrix} = \{\mathbf{F}(t)\} \tag{9}$$

where

$$\begin{aligned} \{\mathbf{F}(t)\} &= \{\mathbf{F}\}_m + \{\mathbf{F}(t)\}_{am} + \{\mathbf{F}(t)\}_{aT} \\ &= \begin{Bmatrix} -F_1 \\ F_2 \\ F_3 \end{Bmatrix} + \begin{Bmatrix} 0 \\ 0 \\ F_{am}\Omega_m^2 \end{Bmatrix}\sin(\Omega_m t + \phi_m) + \begin{Bmatrix} 0 \\ 0 \\ F_{aT} \end{Bmatrix} \\ &\quad \sin(\Omega_T t + \phi_T) \\ &\zeta_{ii} = c_i/2m_i\omega_n, \quad \zeta_{i3} = c_m/2m_i\omega_n, \quad i = 1, 2, \quad \zeta_{33} = c_m/2m_c\omega_n \\ &k_{ii} = \omega_i^2/\omega_n^2, \quad k_{i3} = m_c/m_i, \quad F_i = \bar{F}_i/m_i b\omega_n^2, \quad i = 1, 2 \\ &F_3 = \bar{F}_3/m_c b\omega_n^2, \quad F_{am} = \tilde{e}/b, \quad F_{aT} = \tilde{F}_{aT}/m_c b\omega_n^2 \end{aligned} \tag{10}$$

in which F_i $(i = 1, 2, 3)$ are dimensionless components included in the mean force vector $\{\mathbf{F}\}_m$, and F_{aT} and F_{am} are dimensionless components pertaining to variable external excitation $\{\mathbf{F}(t)\}_{aT}$ and internal excitation $\{\mathbf{F}(t)\}_{am}$, respectively. Further, the nonlinear functions $f_m(x_3)$ due to gear backlashes and $f_i(x_i)$ caused by clearances of rolling element bearings are defined as

$$f_m(x_3) = \begin{cases} x_3 - b_3/b, & x_3 > b_3/b \\ 0, & -b_3/b < x_3 < b_3/b \\ x_3 + b_3/b, & x_3 < -b_3/b \end{cases} \tag{11}$$

$$f_i(x_i) = \begin{cases} x_i - b_i/b, & x_i > b_i/b \\ 0, & -b_i/b < x_i < b_i/b \\ x_i + b_i/b, & x_i < -b_i/b \end{cases} \tag{12}$$

where b_3 indicates a half backlash, and b_i $(i = 1, 2)$ denotes a half radial clearance of the ith pair bearing.

3 Incremental Harmonic Balance Method for Periodic and Period-Doubling Solutions of the Gear Transmission System

In this section, the steady-state response of the gear transmission system with multipiecewise linear functions is analyzed in detail by employing the IHB method. The IHB method is a reliable methodology to obtain periodic solutions of a system with general nonlinearities or piecewise linearities [27,31], and has been extended to analyze responses of complex multi-DOF nonlinear systems, such as a two-DOF vehicle system [32] and a three-DOF unit-cell system [33].

A time variable is introduced:

$$\tau = \omega t \tag{13}$$

Substituting Eq. (13) into Eq. (9) yields

$$\omega^2 \begin{bmatrix} 1 & 0 & 0 \\ 0 & 1 & 0 \\ -1 & 1 & 1 \end{bmatrix} \begin{Bmatrix} x_1''(\tau) \\ x_2''(\tau) \\ x_3''(\tau) \end{Bmatrix} + 2\omega \begin{bmatrix} \zeta_{11} & 0 & \zeta_{13} \\ 0 & \zeta_{22} & -\zeta_{23} \\ 0 & 0 & \zeta_{33} \end{bmatrix} \begin{Bmatrix} x_1'(\tau) \\ x_2'(\tau) \\ x_3'(\tau) \end{Bmatrix} + \begin{bmatrix} k_{11} & 0 & k_{13} \\ 0 & k_{22} & -k_{23} \\ 0 & 0 & 1 \end{bmatrix} \begin{Bmatrix} f_1(x_1) \\ f_2(x_2) \\ f_m(x_3) \end{Bmatrix} = \{\mathbf{F}(\tau/\omega)\} \tag{14}$$

where $()'$ and $()''$ denote the first and second derivatives with respect to time τ, respectively, and

$$\begin{aligned} \{\mathbf{F}(\tau/\omega)\} &= \{\mathbf{F}\}_m + \{\mathbf{F}(\tau/\omega)\}_{am} + \{\mathbf{F}(\tau/\omega)\}_{aT} \\ &= \begin{Bmatrix} -F_1 \\ F_2 \\ F_3 \end{Bmatrix} + \begin{Bmatrix} 0 \\ 0 \\ F_{am}\Omega_m^2 \end{Bmatrix} \sin(\Omega_m \cdot \tau/\omega + \phi_m) \\ &\quad + \begin{Bmatrix} 0 \\ 0 \\ F_{aT} \end{Bmatrix} \sin(\Omega_T \cdot \tau/\omega + \phi_T) \end{aligned} \tag{15}$$

In order to conveniently formulate the process of the IHB method, Eq. (14) can be written in the matrix form

$$\omega^2 \bar{\mathbf{M}} \mathbf{x}''(\tau) + 2\omega \bar{\mathbf{C}}\, \mathbf{x}'(\tau) + \bar{\mathbf{K}} \mathbf{f}(\mathbf{x}) = \bar{\mathbf{F}}(\tau/\omega) \tag{16}$$

where

$$\begin{aligned} &\bar{\mathbf{M}} = \begin{bmatrix} 1 & 0 & 0 \\ 0 & 1 & 0 \\ -1 & 1 & 1 \end{bmatrix}, \quad \bar{\mathbf{C}} = \begin{bmatrix} \zeta_{11} & 0 & \zeta_{13} \\ 0 & \zeta_{22} & -\zeta_{23} \\ 0 & 0 & \zeta_{33} \end{bmatrix}, \\ &\bar{\mathbf{K}} = \begin{bmatrix} k_{11} & 0 & k_{13} \\ 0 & k_{22} & -k_{23} \\ 0 & 0 & 1 \end{bmatrix} \\ &\mathbf{x}(\tau) = \begin{bmatrix} x_1(\tau) \\ x_2(\tau) \\ x_3(\tau) \end{bmatrix}, \quad \mathbf{f}(\mathbf{x}) = \begin{bmatrix} f_1(x_1) \\ f_2(x_2) \\ f_m(x_3) \end{bmatrix}, \quad \bar{\mathbf{F}}(\tau/\omega) = \{\mathbf{F}(\tau/\omega)\} \end{aligned} \tag{17}$$

The first step of the IHB formulation is the process of incrementation, i.e., the Newton–Raphson procedure. Assume that $\Omega_m = \Omega_T = \omega$, $\phi_m = \phi_T = 0$, and x_{i0} and ω_0 denote the initial state of the system, a vibration state near the initial state can be arrived at by adding small increments to x_{i0} and ω_0:

$$x_i = x_{i0} + \Delta x_i, \quad \omega = \omega_0 + \Delta\omega \tag{18}$$

Substituting Eq. (18) into Eq. (16) and neglecting higher orders of the increments yield the linearized equation

$$\begin{aligned} &\omega_0^2 \bar{\mathbf{M}} \Delta\mathbf{x}'' + 2\omega_0 \bar{\mathbf{C}} \Delta\mathbf{x}' + \bar{\mathbf{K}} \frac{\mathrm{d}\mathbf{f}}{\mathrm{d}\mathbf{x}}\Big|_{\mathbf{x}=\mathbf{x}_0} \Delta\mathbf{x} \\ &\quad = \bar{\mathbf{R}} - 2\left[\omega_0 \bar{\mathbf{M}} \mathbf{x}_0'' + \bar{\mathbf{C}} \mathbf{x}_0' - \omega_0 \bar{\mathbf{F}}_{am} \sin(\tau)\right] \Delta\omega \end{aligned} \tag{19}$$

where

$$\begin{aligned} &\mathbf{x}_0 = \begin{bmatrix} x_{10} \\ x_{20} \\ x_{30} \end{bmatrix}, \quad \Delta\mathbf{x} = \begin{bmatrix} \Delta x_1 \\ \Delta x_2 \\ \Delta x_3 \end{bmatrix} \\ &\bar{\mathbf{R}} = \bar{\mathbf{F}}_m + \omega_0^2 \bar{\mathbf{F}}_{am} \sin(\tau) + \bar{\mathbf{F}}_{aT} \sin(\tau) \\ &\quad - [\omega_0^2 \bar{\mathbf{M}} \mathbf{x}_0'' + 2\omega_0 \bar{\mathbf{C}} \mathbf{x}_0' + \bar{\mathbf{K}} \mathbf{f}(\mathbf{x}_0)] \\ &\text{in which } \bar{\mathbf{F}}_m = \begin{bmatrix} -F_1 \\ F_2 \\ F_3 \end{bmatrix}, \quad \bar{\mathbf{F}}_{am} = \begin{bmatrix} 0 \\ 0 \\ F_{am} \end{bmatrix}, \quad \bar{\mathbf{F}}_{aT} = \begin{bmatrix} 0 \\ 0 \\ F_{aT} \end{bmatrix} \end{aligned} \tag{20}$$

The next step of the IHB formulation is the process of harmonic balance. Under the internal and external excitations, the periodic and period-doubling responses can be obtained by expanding x_{i0} in a truncated Fourier series and utilizing the Galerkin procedure. Thus, x_{i0} and its increments Δx_i described with truncated Fourier series can be written as

$$x_{i0} = \sum_{n=1}^{n_c} a_{i,(n-1)/p} \cos\frac{(n-1)\tau}{p} + \sum_{n=1}^{n_s} b_{i,n/p} \sin\frac{n\tau}{p} = \mathbf{C}_s A_i \tag{21}$$

$$\Delta x_i = \sum_{n=1}^{n_c} \Delta a_{i,(n-1)/p} \cos\frac{(n-1)\tau}{p} + \sum_{n=1}^{n_s} \Delta b_{i,n/p} \sin\frac{n\tau}{p} = \mathbf{C}_s \Delta A_i \tag{22}$$

where

$$\mathbf{C}_s = \left[1 \;\; \cos\frac{\tau}{p} \;\; \cos\frac{2\tau}{p} \cdots \;\; \cos\frac{(n_c-1)\tau}{p} \;\; \sin\frac{\tau}{p} \;\; \sin\frac{2\tau}{p} \;\; \cdots \;\; \sin\frac{n_s\tau}{p}\right] \tag{23}$$

$$A_i = [a_{i,0} \;\; a_{i,1/p} \;\; a_{i,2/p} \;\; \cdots \;\; a_{i,(n_c-1)/p} \;\; b_{i,1/p} \;\; b_{i,2/p} \;\; \cdots \;\; b_{i,n_s/p}]^T \tag{24}$$

$$\begin{aligned} \Delta A_i = [&\Delta a_{i,0} \;\; \Delta a_{i,1/p} \;\; \Delta a_{i,2/p} \;\; \cdots \;\; \Delta a_{i,(n_c-1)/p} \;\; \Delta b_{i,1/p} \\ &\Delta b_{i,2/p} \;\; \cdots \;\; \Delta b_{i,n_s/p}]^T \end{aligned} \tag{25}$$

in which $a_{i,(n-1)/p}$ and $b_{i,n/p}$ denote the Fourier coefficients, n_c and n_s are the numbers of cosine and sine harmonic terms retained, respectively, and p is a positive integer that is introduced for analysis of a potential period-doubling response. In this work, $p = 1$, $n_c = 14$, and $n_s = 13$ indicate a period-1 solution and $n_c = 1 + 13 \cdot p$ and $n_s = 13 \cdot p$ denote a period-p solution, where $p = 1, 2, 4, 8, \ldots$.

The displacement vector $\mathbf{x}_0$ and its increment $\Delta\mathbf{x}$ can thus be expressed by the truncated Fourier coefficient vector $\mathbf{A}$ and its increment $\Delta\mathbf{A}$ as

$$\mathbf{x}_0 = \mathbf{S}\mathbf{A}, \quad \Delta\mathbf{x} = \mathbf{S}\Delta\mathbf{A} \tag{26}$$

respectively, where

$$\mathbf{S} = \mathrm{diag}[\mathbf{C}_s \quad \mathbf{C}_s \quad \cdots \quad \mathbf{C}_s]$$
$$\mathbf{A} = [\mathbf{A}_1^T \quad \mathbf{A}_2^T \quad \cdots \quad \mathbf{A}_n^T]^{\mathrm{T}}, \quad \Delta\mathbf{A} = [\Delta\mathbf{A}_1^T \quad \Delta\mathbf{A}_2^T \quad \cdots \quad \Delta\mathbf{A}_n^T]^T \tag{27}$$

The first and second derivatives of the generalized coordinate vector and its increments that are described by Eq. (26) with respect to time τ can be written as

$$\mathbf{x}_0' = \mathbf{S}'\mathbf{A}, \quad \Delta\mathbf{x}' = \mathbf{S}'\Delta\mathbf{A} \tag{28}$$

$$\mathbf{x}_0'' = \mathbf{S}''\mathbf{A}, \quad \Delta\mathbf{x}'' = \mathbf{S}''\Delta\mathbf{A} \tag{29}$$

respectively.

The process of harmonic balance for one cycle is performed with the Galerkin procedure. By noting that the cycle for the period-p response is $2p\pi$, Eq. (19) becomes

$$\int_0^{2p\pi} \delta(\Delta\mathbf{x})^T \left[\omega_0^2\bar{\mathbf{M}}\Delta\mathbf{x}'' + 2\omega_0\bar{\mathbf{C}}\Delta\mathbf{x}' + \bar{\mathbf{K}}\frac{\mathrm{d}\mathbf{f}}{\mathrm{d}\mathbf{x}}\Big|_{\mathbf{x}=\mathbf{x}_0}\Delta\mathbf{x}\right]\mathrm{d}\tau$$
$$= \int_0^{2p\pi} \delta(\Delta\mathbf{x})^T \left[\bar{\mathbf{R}} - 2\left[\omega_0\mathbf{x}_0'' + \bar{\mathbf{C}}\mathbf{x}_0' - \omega_0\bar{\mathbf{F}}_{am}\sin(\tau)\right]\Delta\omega\right]\mathrm{d}\tau \tag{30}$$

Substituting Eqs. (27)–(29) into Eq. (30) yields a set of linear equations in terms of $\Delta\mathbf{A}$ and $\Delta\omega$

$$\mathbf{K}_{mc}\Delta\mathbf{A} = \mathbf{R} - \mathbf{R}_\omega\Delta\omega \tag{31}$$

where

$$\mathbf{K}_{mc} = \omega_0^2\mathbf{M} + 2\omega_0\mathbf{C} + \mathbf{K}' \tag{32}$$

$$\mathbf{R} = \mathbf{F}_m + \omega_0^2\mathbf{F}_{am} + \mathbf{F}_{aT} - (\omega_0^2\mathbf{M}\mathbf{A} + 2\omega_0\mathbf{C}\mathbf{A} + \mathbf{R}^K) \tag{33}$$

$$\mathbf{R}_\omega = 2(\omega_0\mathbf{M}\mathbf{A} + \mathbf{C}\mathbf{A} - \omega_0\mathbf{F}_{am}) \tag{34}$$

in which

$$\begin{aligned}
\mathbf{M} &= \int_0^{2p\pi} \mathbf{S}^T\bar{\mathbf{M}}\mathbf{S}''\mathrm{d}\tau, \quad \mathbf{C} = \int_0^{2p\pi} \mathbf{S}^T\bar{\mathbf{C}}\mathbf{S}'\mathrm{d}\tau \\
\mathbf{R}^K &= \int_0^{2p\pi} \mathbf{S}^T\bar{\mathbf{K}}\mathbf{f}(\mathbf{x}_0)\mathrm{d}\tau, \quad \mathbf{K}' = \int_0^{2p\pi} \mathbf{S}^T\bar{\mathbf{K}}\frac{\mathrm{d}\mathbf{f}}{\mathrm{d}\mathbf{x}}\Big|_{\mathbf{x}=\mathbf{x}_0}\mathbf{S}\mathrm{d}\tau \\
\mathbf{F}_m &= \int_0^{2p\pi} \mathbf{S}^T\bar{\mathbf{F}}_m\mathrm{d}\tau, \quad \mathbf{F}_{am} = \int_0^{2p\pi} \mathbf{S}^T\bar{\mathbf{F}}_{am}\sin\tau\mathrm{d}\tau, \\
\mathbf{F}_{aT} &= \int_0^{2p\pi} \mathbf{S}^T\bar{\mathbf{F}}_{aT}\sin\tau\mathrm{d}\tau
\end{aligned} \tag{35}$$

It is worth noting that the piecewise linear stiffness matrix $\mathbf{K}'$ and vector $\mathbf{R}^K$ cannot be integrated by direct numerical integration in the cycle $2p\pi$ since displacements in radial and torsional directions are piecewise linear functions, and their calculation process is different from that of other matrices, like the mass matrix $\mathbf{M}$ and damping matrix $\mathbf{C}$. The detailed procedures for calculating the stiffness matrix $\mathbf{K}'$ and vector $\mathbf{R}^K$ are given by

$$\mathbf{K}' = \begin{bmatrix} [\mathbf{K}_{11}'] & [\mathbf{K}_{12}'] & [\mathbf{K}_{13}'] \\ [\mathbf{K}_{21}'] & [\mathbf{K}_{22}'] & [\mathbf{K}_{23}'] \\ [\mathbf{K}_{31}'] & [\mathbf{K}_{32}'] & [\mathbf{K}_{33}'] \end{bmatrix}, \quad \mathbf{R}^K = \begin{bmatrix} \mathbf{R}_1^K \\ \mathbf{R}_2^K \\ \mathbf{R}_3^K \end{bmatrix},$$
$$\mathbf{R}_i^K = [\mathbf{K}_{ij}']\mathbf{A}_i + [\mathbf{R}_{ij}]^{NL}b_i, \quad (i,j = 1,2,3) \tag{36}$$

where

$$\begin{aligned}
\left[\mathbf{K}_{ij}'\right]_{s,t} &= \frac{1}{2}\bar{\mathbf{K}}_{ij}\sum_{k=0}^{1+m1} H_m(k)p\left[\frac{\sin\big((s+t-2)/p\big)\alpha(k+1) - \sin\big((s+t-2)/p\big)\alpha(k)}{s+t-2}\right. \\
&\quad \left. + \frac{\sin\big((s-t)/p\big)\alpha(k+1) - \sin\big((s-t)/p\big)\alpha(k)}{s-t}\right], (s = 1,2,\ldots,n_c, t = 1,2,\ldots,n_c) \\
\left[\mathbf{K}_{ij}'\right]_{s,t+n_c} &= -\frac{1}{2}\bar{\mathbf{K}}_{ij}\sum_{k=0}^{1+m1} H_m(k)p\left[\frac{\cos\big((s+t-1)/p\big)\alpha(k+1) - \cos\big((s+t-1)/p\big)\alpha(k)}{t-s+1}\right. \\
&\quad \left. - \frac{\cos\big((t-s+1)/p\big)\alpha(k+1) - \cos\big((t-s+1)/p\big)\alpha(k)}{t-s+1}\right] \\
\left[\mathbf{K}_{ij}'\right]_{s+n_c,t} &= -\frac{1}{2}\bar{\mathbf{K}}_{ij}\sum_{k=0}^{1+m1} H_m(k)p\left[\frac{\cos\big((s+t-1)/p\big)\alpha(k+1) - \cos\big((s+t-1)/p\big)\alpha(k)}{s+t-1}\right. \\
&\quad \left. + \frac{\cos\big((s-t+1)/p\big)\alpha(k+1) - \cos\big((s-t+1)/p\big)\alpha(k)}{s-t+1}\right] \\
\left[\mathbf{K}_{ij}'\right]_{s+n_c,t+n_c} &= -\frac{1}{2}\bar{\mathbf{K}}_{ij}\sum_{k=0}^{1+m1} H_m(k)p\left[\frac{\sin((s+t)/p)\alpha(k+1) - \sin((s+t)/p)\alpha(k)}{s+t}\right. \\
&\quad \left. + \frac{\sin\big((s-t)/p\big)\alpha(k) - \sin\big((s-t)/p\big)\alpha(k+1)}{s-t}\right] \\
[\mathbf{R}_{ij}]_s^{NL} &= \bar{\mathbf{K}}_{ij}\sum_{k=0}^{1+m1} H_m(k)S_m(k)p\left[\frac{\sin\big((s-1)/p\big)\alpha(k+1) - \sin\big((s-1)/p\big)\alpha(k)}{s-1}\right] \\
[\mathbf{R}_{ij}]_{s+n_c}^{NL} &= \bar{\mathbf{K}}_{ij}\sum_{k=0}^{1+m1} H_m(k)S_m(k)p\left[\frac{\cos(s/p)\alpha(k) - \cos(s/p)\alpha(k+1)}{s}\right]
\end{aligned} \tag{37}$$

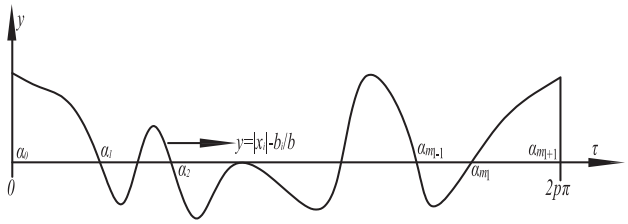

Fig. 2 Zeros of the equation $y = |x_i| - b_i/b$

in which $m1$ is the number of zeros of the equation $|x_i| = b_i/b$ within the interval $[0 \quad 2p\pi]$; $\alpha_0 = 0$, $\alpha_{1+m1} = 2p\pi$, and $\alpha_1, \alpha_2, \ldots, \alpha_{m1}$ $(\alpha_1 < \alpha_2 < \cdots < \alpha_{m1})$ are zeros of the equation $|x_i| = b_i/b$, as shown in Fig. 2, which can be calculated in an iteration through a procedure that uses bisection and interpolation methods on the trigonometric equation $|x_i| = b_i/b$; H_m and S_m are step functions that are expressed as

$$H_m(k) = \begin{cases} 1, & u_k \geq 0 \\ 0, & u_k < 0 \end{cases} \tag{38}$$

$$S_m(k) = \begin{cases} -1, & v_k \geq 0 \\ 1, & v_k < 0 \end{cases} \tag{39}$$

respectively, with $k = 0, 1, 2, \ldots, m1$; and $u_0, u_1, u_2, \ldots, u_k$ and $v_0, v_1, v_2, \ldots, v_k$ denote values of sign functions $|x_i| = b_i/b$ and $x_i = b_i/b$ in the subintervals $[\alpha_0 \quad \alpha_1], [\alpha_1 \quad \alpha_2], \ldots, [\alpha_{m1} \quad \alpha_{1+m1}]$, respectively.

In order to obtain a periodic or period-doubling solution of Eq. (31), an initial state should first be given, which is not necessarily required to be an accurate solution. A steady-state response is obtained as long as the initialization procedure converges to an accurate solution through the iterative procedure. The norm of $\mathbf{R}$ in the iterative procedure is set to be less than a given tiny value $\varepsilon = 1.0 \times 10^{-9}$ in this work. Three options of an incrementation process, i.e., the frequency increment, the amplitude increment, and the arc-length increment, for tracing a frequency response curve can be utilized, which are described in Ref. [34].

4 Analysis of Stability for Periodic and Period-Doubling Solutions and Bifurcation Type

The Floquet theory is developed in this section to analyze stability of a piecewise linear system. When the periodic steady-state solution $\mathbf{x}_0$ of the gear transmission system is obtained by the IHB method, stability and the bifurcation type of the periodic or period-doubling solution can be investigated by applying the Floquet theory [34]. The first step of stability analysis is to add a small perturbation $\Delta\mathbf{x}$ to $\mathbf{x}_0$:

$$\mathbf{x} = \mathbf{x}_0 + \Delta\mathbf{x} \tag{40}$$

Substituting Eq. (40) into Eq. (16) and neglecting higher-order incremental terms, one can obtain the linearized equation with $\Delta\mathbf{x}$ as an unknown

$$\omega^2\bar{\mathbf{M}}\Delta\ddot{\mathbf{x}} + 2\omega\bar{\mathbf{C}}\Delta\dot{\mathbf{x}} + \bar{\mathbf{K}}\mathbf{f}'(\mathbf{x}_0)\Delta\mathbf{x} = 0 \tag{41}$$

Equation (41) is the perturbed equation from the equilibrium state $\mathbf{x}_0$ [35]. Stability of the periodic or period-doubling solution of Eq. (41) can be investigated by employing the Floquet theory in the cycle $2p\pi$. By defining

$$\mathbf{q} = [\Delta\mathbf{x} \quad \Delta\dot{\mathbf{x}}]^T \tag{42}$$

Equation (41) can be expressed in the state-space form as

$$\dot{\mathbf{q}} = \mathbf{Q}(\tau)\mathbf{q} \tag{43}$$

where

$$\mathbf{Q} = \begin{bmatrix} \mathbf{0} & \mathbf{I} \\ \mathbf{Q}_{21}(\tau) & \mathbf{Q}_{22} \end{bmatrix} \tag{44}$$

in which

$$\mathbf{Q}_{21} = -\bar{\mathbf{M}}^{-1}\frac{\bar{\mathbf{K}}\mathbf{f}'(\mathbf{x}_0)}{\omega^2} \tag{45}$$

$$\mathbf{Q}_{22} = -2\bar{\mathbf{M}}^{-1}\frac{\bar{\mathbf{C}}}{\omega} \tag{46}$$

and $\mathbf{I}$ is the n-order identity matrix, and $\mathbf{0}$ is the n-order zero matrix. Since each element of the column vector $\mathbf{x}_0$ is a periodic function of dimensionless time τ with period $T = 2p\pi$ with p denoting the period-p solution, each component of $\mathbf{Q}_{21}$ is a periodic function as well and its cycle is the same as that of $\mathbf{q}_0$. Therefore, $\mathbf{Q}$ is a periodic $2n$-order square matrix whose period is T.

For Eq. (43), there exists a set of fundamental solutions

$$\mathbf{z}_l = [z_{1l} \quad z_{2l} \quad \cdots \quad z_{Nl}]^T, \quad l = 1, 2, \ldots, 2n \tag{47}$$

where $N = 2n$. This fundamental solution set can be expressed in the matrix form

$$\mathbf{Z} = \begin{bmatrix} z_{11} & z_{12} & \cdots & z_{1N} \\ z_{21} & z_{22} & \cdots & z_{2N} \\ \vdots & \vdots & & \vdots \\ z_{N1} & z_{N2} & \cdots & z_{NN} \end{bmatrix} \tag{48}$$

which satisfies the matrix equation

$$\dot{\mathbf{Z}} = \mathbf{Q}(\tau)\mathbf{Z} \tag{49}$$

Since $\mathbf{Q}(\tau)$ is a periodic function with period T, i.e., $\mathbf{Q}(\tau) = \mathbf{Q}(\tau + T)$, $\mathbf{Z}(\tau)$ is also a fundamental matrix solution with period T. Thus, $\mathbf{Z}(\tau)$ can be expressed as

$$\mathbf{Z}(\tau) = \mathbf{P}\mathbf{Z}(\tau + T) \tag{50}$$

where $\mathbf{P}$ is called the transition matrix that is a nonsingular constant matrix. According to the Floquet theory, stability of the system depends on eigenvalues of the transition matrix $\mathbf{P}$. If all moduli of the eigenvalues of $\mathbf{P}$ are smaller than 1, the motion of the gear transmission system is bounded and the periodic or period-doubling solution is stable; otherwise, the motion is unbounded and the solution is unstable. The key to stability analysis is evaluation of the transition matrix with an efficient method. An effective method for approximating the transition matrix has been proposed by Hsu [36,37] and it has been improved by the precise Hsu's method [38]. The period T is divided into a large number of equal subintervals, and the integration over each equal part is operated with the method developed by Hsu [36]. In this work, the period $T = 2p\pi$ is divided into L equal subintervals indicated by τ_l, where $l = 1, 2, \ldots, L+2$, with $\tau_1 < \tau_2 < \cdots < \tau_{L+2}$, where $\tau_1 = 0$ and $\tau_{L+2} = 2p\pi$ with $L = p \cdot 10000$. The size of the lth subinterval is

$$\Delta_l = \tau_l - \tau_{l-1} \tag{51}$$

Define the step function U_m as

$$U_m(l) = \begin{cases} 1, & u_l \geq 0 \\ 0, & u_l < 0 \end{cases} \tag{52}$$

where $u_1, u_2, \ldots, u_l$ denote values of the sign function $|x_i| = b_i/b$ in the subintervals $[\tau_1 \quad \tau_2], [\tau_2 \quad \tau_3], \cdots, [\tau_{L+1} \quad \tau_{L+2}]$, respectively.

In the lth equal part, the periodic coefficient matrix $\mathbf{Q}(\tau)$ is substituted with the constant quotient matrix $\mathbf{Q}_l$ defined as

$$\mathbf{Q}_l = \begin{bmatrix} \mathbf{0} & \mathbf{I} \\ [\mathbf{Q}_{21}]_l & [\mathbf{Q}_{22}]_l \end{bmatrix} \tag{53}$$

where

$$\begin{aligned} [\mathbf{Q}_{21}]_l &= -U_m(l)\frac{1}{\Delta_l}\int_{\tau_{l-1}}^{\tau_l} \bar{\mathbf{M}}^{-1}\frac{\bar{\mathbf{K}}}{\omega^2}\mathrm{d}\tau, \\ [\mathbf{Q}_{22}]_l &= -2\frac{1}{\Delta_l}\int_{\tau_{l-1}}^{\tau_l} \bar{\mathbf{M}}^{-1}\frac{\bar{\mathbf{C}}}{\omega}\mathrm{d}\tau \end{aligned} \tag{54}$$

Finally, the transition matrix is expressed as

$$\mathbf{P} = \mathbf{Z}(T) = \prod_{l=1}^{L}\left[\mathbf{I} + \sum_{r=1}^{R}\frac{(\Delta_l \mathbf{Q}_l)^r}{r!}\right] \tag{55}$$

where R is the number of truncated terms in the Taylor expansion.

For a periodic system with period T, stability of periodic solutions is related to the way of Floquet multipliers moving outside the unit circle [39]. Three typical manners of moving outside the unit circle are described here. First, there exists a pair of complex conjugates for the Floquet multipliers and their moduli are not less than 1, which indicates that the Floquet multipliers leave the unit circle by the manner of complex conjugates, causing Hopf bifurcation. In this case, a quasi-periodic response appears near the bifurcation point. Second, there are positive real values for the Floquet multipliers and one of its moduli is not less than 1, which indicates that the Floquet multipliers move outside the unit circle through the $+1$ direction along the real axis, resulting in three types of bifurcations: (a) saddle-node bifurcation, where the response jumps from a stable solution to another stable solution around the bifurcation point; (b) symmetry-breaking bifurcation, where symmetry of the periodic solution is broken by the response; and (c) transcritical bifurcation, where stability of the periodic solution is exchanged. Third, there are negative real values for the Floquet multipliers and one of its moduli is not less than 1, which indicates that the Floquet multipliers leave the unit circle through the –1 direction along the real axis, resulting in period-doubling bifurcation. In this case, the period-2^{n-1} response exists near the bifurcation point, where n is an integer that is greater than 1 [40].

5 Numerical Results and Discussion

In this section, primary, superharmonic, and subharmonic resonances, various bifurcation types, and period-doubling responses of the gear transmission system subjected to internal and external excitations are discussed. Note that curves of nonlinear frequency responses of the first and second DOFs are same, which is caused by the opposite direction of external excitation acting on the first and second DOFs. Thus, the nonlinear frequency response curve of the second DOF is not presented in this work. The main parameters of the gear transmission system are same as those in Ref. [29] with $m_i = 1\text{kg}$, $r_i = 0.04\text{m}$, $I_i = 0.0008\,\text{kg/m}^2$, $k_i = 1\times 10^9\text{N/m}\,(i = 1,2)$, and $k_m = 2\times 10^8\text{N/m}$; the primary dimensionless matrices of the system are then obtained as follows:

$$\begin{aligned} \bar{\mathbf{M}} &= \begin{bmatrix} 1 & 0 & 0 \\ 0 & 1 & 0 \\ -1 & 1 & 1 \end{bmatrix}, \quad \bar{\mathbf{C}} = \begin{bmatrix} 0.01 & 0 & 0.0125 \\ 0 & 0.01 & -0.0125 \\ 0 & 0 & 0.05 \end{bmatrix}, \\ \bar{\mathbf{K}} &= \begin{bmatrix} 1.25 & 0 & 0.25 \\ 0 & 1.25 & -0.25 \\ 0 & 0 & 1 \end{bmatrix} \\ \bar{\mathbf{F}}_1 &= \begin{bmatrix} 0 \\ 0 \\ 0.1 \end{bmatrix}, \quad \bar{\mathbf{F}}_{ah} = \begin{bmatrix} 0 \\ 0 \\ 0.05 \end{bmatrix}, \quad \bar{\mathbf{F}}_{aT} = \begin{bmatrix} 0 \\ 0 \\ 0.05 \end{bmatrix}, \\ \bar{\mathbf{b}} &= \begin{bmatrix} b_1 \\ b_2 \\ b_m \end{bmatrix} = \begin{bmatrix} 0 \\ 0 \\ 1 \end{bmatrix} \end{aligned} \tag{56}$$

The number of cosine harmonic terms is n_c and the number of sine harmonic terms is n_s. Equation (21) can be written as

$$x_{i0} = a_{i,0} + \sum_{n=1}^{n_s} A_{i,n/p}\cos((n/p)\tau + \phi_{i,n/p}), \quad i = 1,2,3 \tag{57}$$

where

$$A_{i,n/p} = \sqrt{a_{i,n/p}^2 + b_{i,n/p}^2}, \quad \phi_{i,n/p} = \text{atan2}(-b_{i,n/p}, a_{i,n/p}) \tag{58}$$

in which $A_{i,n/p}$ and $\phi_{i,n/p}$ denote the amplitude and phase angle of the (n/p)th-order harmonic term for the ith DOF, respectively. And the amplitude A_i of each DOF can be described as

$$A_i = a_{i,0} + \sum_{j=0}^{n_s}\sqrt{a_{i,j/p}^2 + b_{i,j/p}^2}, \quad (i = 1,2,3) \tag{59}$$

5.1 Analysis of Nonlinear Phenomena and Resonances by Considering Different Numbers of DOFs. Figure 3 exhibits first two order harmonic frequency response curves of the third DOF by considering different numbers of DOFs, where j denotes the total number of DOFs considered, i.e., $j=1$, $j=2$, and $j=3$ denotes one DOF (the third DOF x_3), two DOFs (the second DOF x_2 and the third DOF x_3), and three DOFs (the first DOF x_1, the second DOF x_2, and the third DOF x_3) considered in the system, respectively. The higher-order harmonic frequency responses are small and not shown here. For $j=1$, there is a peak on each of the two frequency response curves $\omega \sim A_{3,1}$ and $\omega \sim A_{3,2}$ marked as "PR," which represents primary resonance, and the frequency response curves $\omega \sim A_{3,1}$ and $\omega \sim A_{3,2}$ display softening-spring nonlinear behaviors that are characterized by response curves bent to the left due to the piecewise linear function $f(x_3)$, as shown in Fig. 3. For $j=2$, according to the primary dimensionless matrices, the third natural frequency ω_{n3} is 1.344. There are three peaks on the frequency response curves $\omega \sim A_{3,1}$ and $\omega \sim A_{3,2}$, as shown in Fig. 3. The left peaks of $\omega \sim A_{3,1}$ and $\omega \sim A_{3,2}$ are near $\omega = 0.45$. The middle peaks of $\omega \sim A_{3,1}$ and $\omega \sim A_{3,2}$ are near $\omega = 0.62$. The right peaks of $\omega \sim A_{3,1}$ and $\omega \sim A_{3,2}$ are near $\omega = 1.22$. The frequency response curve $\omega \sim A_{3,1}$ displays softening-spring behaviors at the three peaks, and the frequency response curve $\omega \sim A_{3,2}$ exhibits a softening-spring behavior at the right peak. It can be seen that there exist primary and superharmonic resonances on the frequency response curves $\omega \sim A_{3,1}$ and $\omega \sim A_{3,2}$ marked as "SP-HR." For $j=3$, according to the primary dimensionless matrices, the third natural frequency ω_{n3} is 1.47. There are three peaks on the frequency response curves $\omega \sim A_{3,1}$ and $\omega \sim A_{3,2}$, as shown in Fig. 3. The left peaks of $\omega \sim A_{3,1}$ and $\omega \sim A_{3,2}$ are near $\omega = 0.45$. The middle peaks of $\omega \sim A_{3,1}$ and $\omega \sim A_{3,2}$ are near $\omega = 0.64$. The right peaks of $\omega \sim A_{3,1}$ and

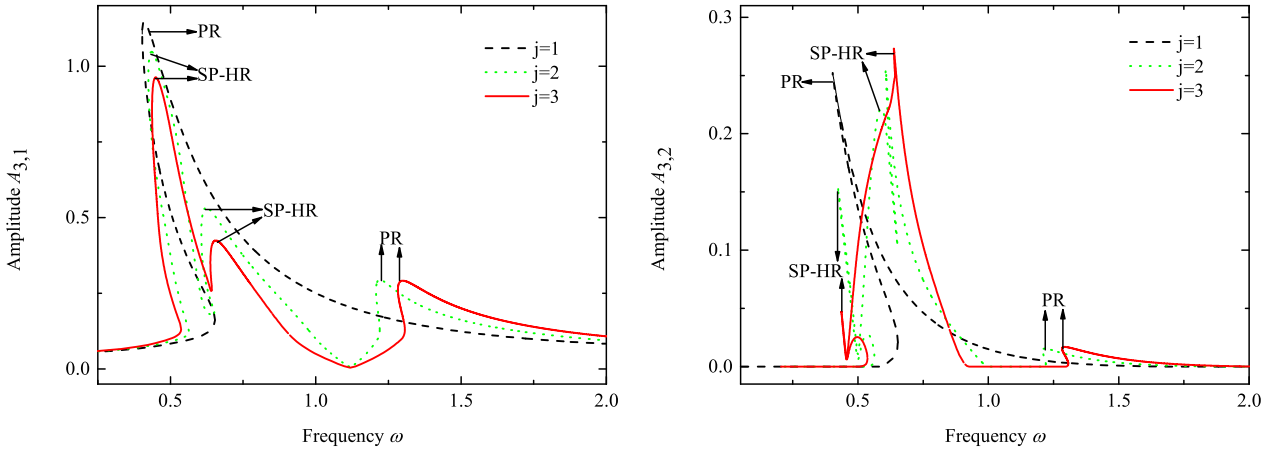

(*a*) (*b*)

Fig. 3 First- and second-order harmonic frequency response curves of the third DOF by considering a one-DOF model (the third DOF x_3), a two-DOF model (the second DOF x_2 and the third DOF x_3), and a three-DOF model (the first DOF x_1, the second DOF x_2, and the third DOF x_3): (*a*) the first-order harmonic frequency response curves and (*b*) the second-order harmonic frequency response curves

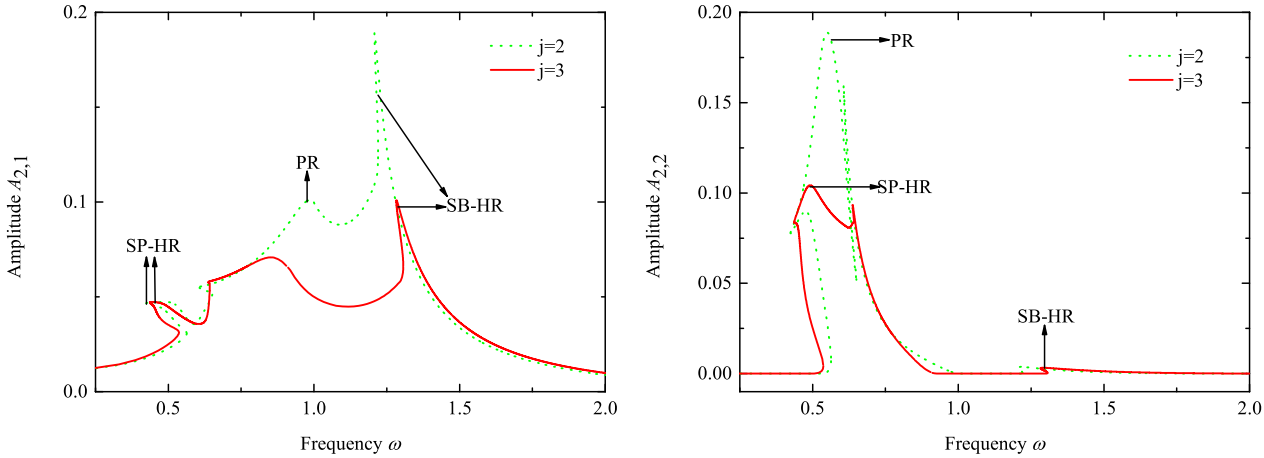

(*a*) (*b*)

Fig. 4 First- and second-order harmonic frequency response curves of the second DOF by considering a two-DOF model (the second DOF x_2 and the third DOF x_3) and a three-DOF model (the first DOF x_1, the second DOF x_2, and the third DOF x_3): (*a*) the first-order harmonic frequency response curves and (*b*) the second-order harmonic frequency response curves

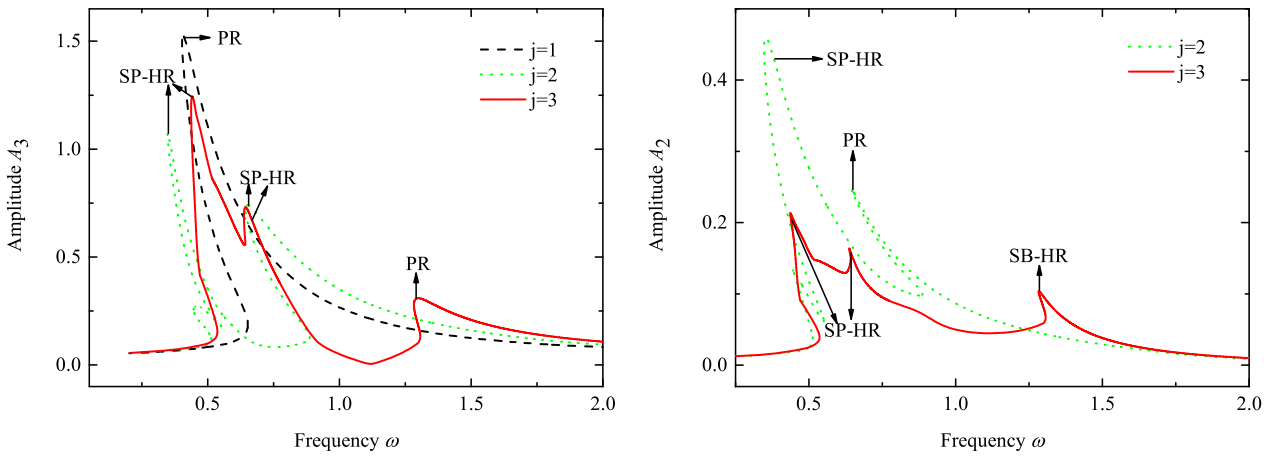

(*a*) (*b*)

Fig. 5 Frequency response curves of the second DOF and the third DOF by considering a two-DOF model (the second DOF x_2 and the third DOF x_3) and a three-DOF model (the first DOF x_1, the second DOF x_2, and the third DOF x_3): (*a*) the frequency response curves of the third DOF and (*b*) the frequency response curves of the second DOF

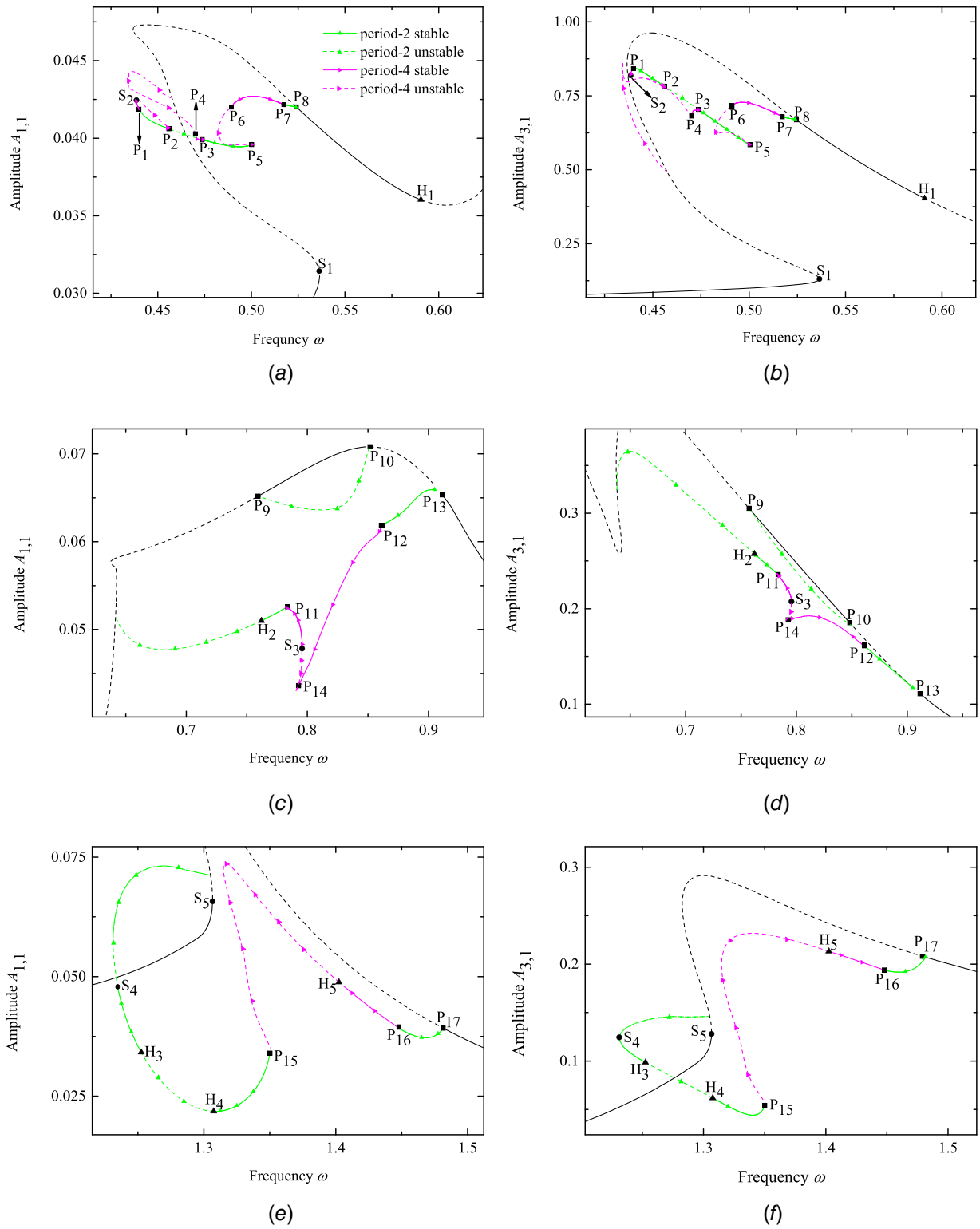

Fig. 6 Bifurcations on the first-order harmonic frequency response curves of the first and third DOFs when the frequency ω is in the region: (*a*) and (*b*) $[0.42, 0.65]$, (*c*) and (*d*) $[0.62, 0.95]$, and (*e*) and (*f*) $[1.22, 1.51]$

$\omega \sim A_{3,2}$ are near $\omega = 1.30$. The frequency response curve $\omega \sim A_{3,1}$ displays softening-spring behaviors at the three peaks, and the frequency response curve $\omega \sim A_{3,2}$ exhibits a softening-spring behavior at the right peak. It can be seen that the frequency response curves $\omega \sim A_{3,1}$ and $\omega \sim A_{3,2}$ display primary and super-harmonic resonances. Further, a comparison of the first two order harmonic frequency response curves for $j = 1$, $j = 2$, and $j = 3$ show that there only exists a primary resonance on the curves $\omega \sim A_{3,1}$ and $\omega \sim A_{3,2}$ when $j = 1$, and the curves $\omega \sim A_{3,1}$ and $\omega \sim A_{3,2}$ display more resonances and nonlinear phenomena as more DOFs are considered, which is caused by coupling of piecewise linear stiffnesses among DOFs. There is no subharmonic resonance on the frequency response curve of the third DOF.

Figure 4 displays the first two order harmonic frequency response curves of the second DOF for $j = 2$ (the second DOF x_2

Table 1 Floquet multipliers for different frequencies near bifurcation points S_1, H_1, and P_8 on the frequency response curves in Fig. 6(*a*)

	ω	First and second Floquet multipliers λ_1, λ_2	Third and fourth Floquet multipliers λ_3, λ_4	Fifth and sixth Floquet multipliers λ_5, λ_6	Moduli of λ_5, λ_6
Near point S_1	0.53622	$-0.53724 \pm 0.22781\bar{i}$	$0.76577 \pm 0.45242\bar{i}$	1.45632, 0.27510	1.45632, 0.27510
	0.53642	$-0.52633 \pm 0.23159\bar{i}$	$0.76802 \pm 0.44865\bar{i}$	0.42044, 0.98208	0.42044, 0.98208
Near point H_1	0.59049	$0.70445 \pm 0.55863\bar{i}$	$0.08115 \pm 0.39709\bar{i}$	$0.32928 \pm 0.94283\bar{i}$	0.99868, 0.99868
	0.59099	$0.69885 \pm 0.56574\bar{i}$	$-0.07845 \pm 0.39677\bar{i}$	$0.32992 \pm 0.94565\bar{i}$	1.00154, 1.00154
Near point P_8	0.52399	$0.59255 \pm 0.66004\bar{i}$	$0.33567 \pm 0.70538\bar{i}$	–1.00273, –0.21283	1.00273, 0.21283
	0.52499	$0.60101 \pm 0.65249\bar{i}$	$0.33410 \pm 0.70799\bar{i}$	–0.99087, –0.21487	0.99087, 0.21487

and the third DOF x_3) and $j=3$ (the first DOF x_1, the second DOF x_2, and the third DOF x_3) considered in the system. For $j=2$, according to the primary dimensionless matrices, the second natural frequency ω_{n2} is 0.831. There exist three peaks on the curve $\omega \sim A_{2,1}$, as shown in Fig. 4(*a*). The left, middle, and right peaks of $\omega \sim A_{2,1}$ are near $\omega = 0.45$, $\omega = 0.99$, and $\omega = 1.22$, respectively. The left peak of the frequency response curve $\omega \sim A_{2,1}$ exhibits a softening-spring behavior that is characterized by the response curve bent to the left due to the piecewise linear function $f(x_2)$. In Fig. 4(*b*), there is a peak on the curve $\omega \sim A_{2,2}$ near $\omega = 0.55$. It can be seen that there are primary, superharmonic, and subharmonic resonances on the frequency response curve $\omega \sim A_{2,1}$ marked as "SB-HR," and there only exists a primary resonance on the curve $\omega \sim A_{2,2}$. For $j=3$, according to the primary dimensionless matrices, the second natural frequency ω_{n2} is 1.118. There are three peaks on the curves $\omega \sim A_{2,1}$ and $\omega \sim A_{2,2}$, as shown in Fig. 4. The left peaks of $\omega \sim A_{2,1}$ and $\omega \sim A_{2,2}$ are near $\omega = 0.45$ and $\omega = 0.50$, respectively. The middle peaks of $\omega \sim A_{2,1}$ and $\omega \sim A_{2,2}$ are near $\omega = 0.86$ and $\omega = 0.64$, respectively. The right peaks of $\omega \sim A_{2,1}$ and $\omega \sim A_{2,2}$ are near $\omega = 1.30$. The frequency response curve $\omega \sim A_{2,1}$ exhibits softening-spring behaviors at the left and right peaks, and the frequency response curve $\omega \sim A_{2,2}$ displays a softening-spring behavior at the right peak. It can be seen that the frequency response curves $\omega \sim A_{2,1}$ and $\omega \sim A_{2,2}$ exhibit superharmonic and subharmonic resonances, respectively. Further, a comparison of the first two order harmonic frequency response curves for $j=2$ and $j=3$ shows that the amplitudes for considering three DOFs are less than those for considering two DOFs in some regions.

Figure 5 shows frequency response curves $\omega \sim A_3$ and $\omega \sim A_2$ of the second and third DOFs by considering different numbers of DOFs, where A_3 and A_2 are amplitudes of the third DOF x_3 and the second DOF x_2, respectively. For $j=1$, the frequency response curve $\omega \sim A_3$ exhibits a primary resonance at the peak and displays a softening-spring behavior, as shown in Fig. 5(*a*). For $j=2$, the frequency response curve $\omega \sim A_3$ exhibits superharmonic resonances at the two peaks and displays softening-spring behaviors. For $j=3$, the frequency response curve $\omega \sim A_3$ exhibits primary and superharmonic resonances at the three peaks and displays softening-spring behaviors. For $j=2$, the frequency response curve $\omega \sim A_2$ exhibits primary and superharmonic resonances at the two peaks and displays softening-spring behaviors, as shown in Fig. 5(*b*). For $j=3$, the frequency response curve $\omega \sim A_2$ exhibits superharmonic and subharmonic resonances at the three peaks and displays softening-spring behaviors.

5.2 Bifurcation Analysis. Figure 6 exhibits bifurcations of period-1, period-2, and period-4 frequency response curves of the first-order harmonics for the first and third DOFs when the frequency ω is in the regions $[0.42, 0.65]$, $[0.62, 0.95]$, and $[1.22, 1.51]$. Unless otherwise specified, in all the frequency response curves below, the symbols "●", "▲", and "■" indicate saddle-node, Hopf, and period-doubling bifurcation points, respectively.

In Figs. 6(*a*) and 6(*b*), there exists a saddle-node bifurcation point S_1, a Hopf bifurcation point H_1, and a period-doubling bifurcation point P_8 on the period-1 nonlinear frequency response curve. For the period-1 nonlinear frequency responses of the first and third DOFs, Eq. (21) can be expressed as

$$x_{10} = \sum_{n=1}^{14} a_{1,n-1} \cos(n-1)\tau + \sum_{n=1}^{13} b_{1,n} \sin n\tau \tag{60}$$

$$x_{30} = \sum_{n=1}^{14} a_{3,n-1} \cos(n-1)\tau + \sum_{n=1}^{13} b_{3,n} \sin n\tau \tag{61}$$

At the point S_1, the period-1 solution becomes unstable and causes a jump phenomenon from a stable solution to another stable solution, as evidenced by a real Floquet multiplier leaving the unit circle through the +1 direction along the real axis (Table 1, where $\bar{i}=\sqrt{-1}$). At the point P_8, the period-1 solution loses its stability as evidenced by a real Floquet multiplier moving away from the unit circle through the –1 direction along the real axis (Table 1), and gets into a period-2 motion. At the point H_1, the period-1 solution loses its stability as evidenced by a pair of complex conjugate Floquet multipliers moving outside the unit circle (Table 1), and results in a quasi-periodic response. One can see that the stable period-2 nonlinear frequency response curve is generated at the period-doubling bifurcation point P_8 that is defined as the supercritical period-doubling bifurcation. In Figs. 6(*a*) and 6(*b*), there are five period-doubling bifurcation points P_1, P_2, P_3, P_5, and P_7 on the period-2 nonlinear frequency response curve, a saddle-node bifurcation point S_2, and two period-doubling bifurcation points P_4 and P_6 on the period-4 nonlinear frequency response curve. On the period-2 frequency response curve, the unstable period-4 response curve is engendered through the period-doubling bifurcation point P_5, which is defined as the subcritical period-doubling bifurcation, and the stable period-4 response curves are generated at the period-doubling bifurcation points P_1, P_2, P_3, and P_7 that are supercritical period-doubling bifurcations. When the system undergoes the subcritical period-doubling bifurcation point P_5, the period-4 solution loses its stability in the region from the point P_5 to P_6. However, when the system undergoes the supercritical period-doubling bifurcation point P_7, the period-4 solution is stable in the region from the point P_7 to P_6 as moduli of all the Floquet multipliers are less than 1. Figure 7 exhibits phase-plane diagrams and Fourier spectra of the period-1 solution when $\omega = 0.77424$ for the three DOFs in Figs. 6(*c*) and 6(*d*), respectively, where solid lines and circles denote period-1 solutions calculated by employing the IHB method and the fourth-order RK method, respectively. From Figs. 7(*a*), 7(*c*), and 7(*e*), one can conclude that the period-1 response is one cycle and the result obtained from the IHB method agrees very well with that obtained from numerical integration. One can see from the Fourier spectra displayed in Figs. 7(*b*), 7(*d*), and 7(*f*) that there are many peaks that are integer multiples of $\omega = 0.77424$.

In Figs. 6(*c*) and 6(*d*), there are three period-doubling bifurcation points P_9, P_{10}, and P_{13} on the period-1 frequency response curve, on which period-1 solutions become unstable as evidenced by a real Floquet multiplier moving away from the unit circle

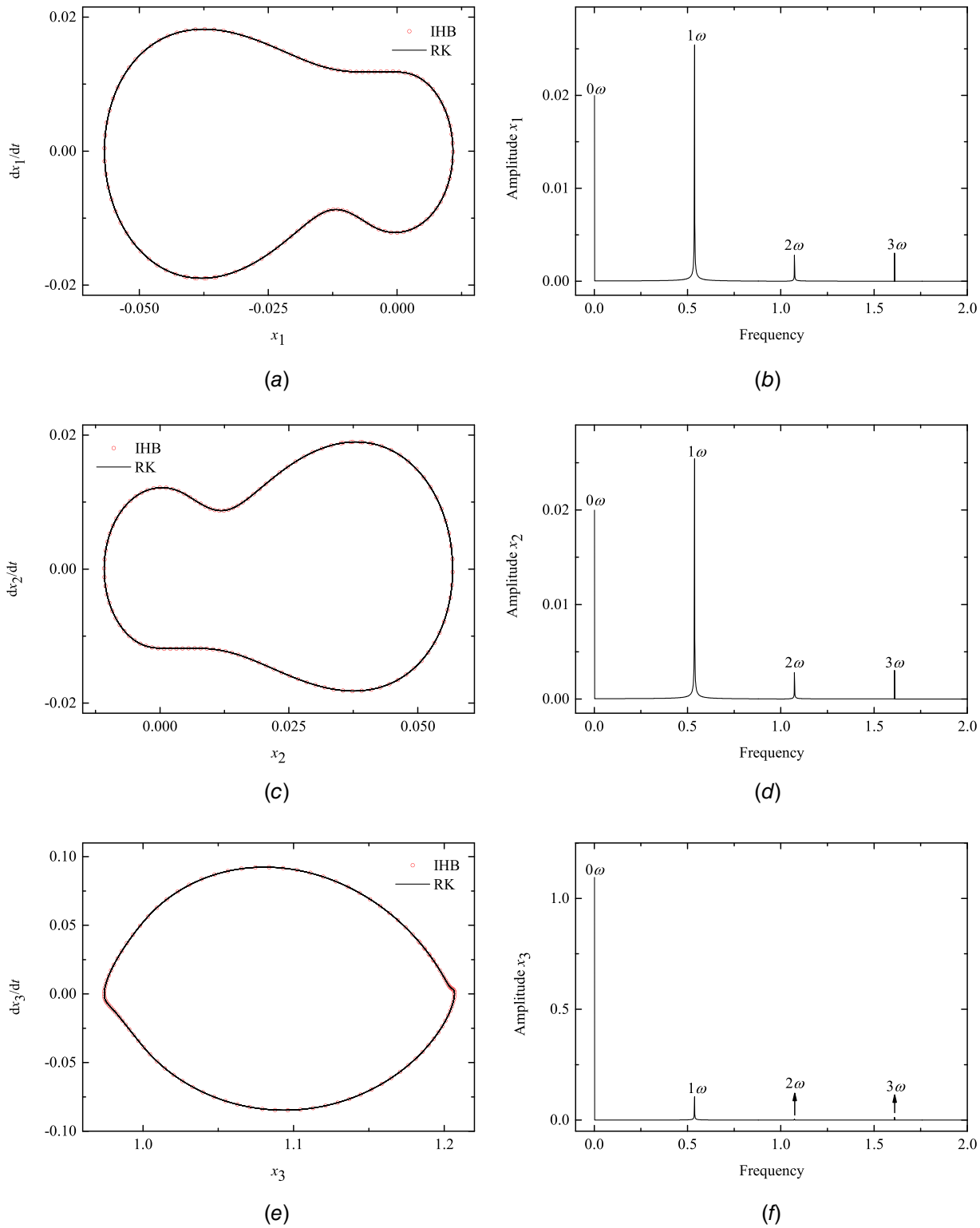

Fig. 7 Period-1 solution as $\omega = 0.77424$ for the three DOFs in Figs. 6(*c*) and 6(*d*): (*a*) phase-plane diagram and (*b*) Fourier spectrum for the first DOF; (*c*) phase-plane diagram and (*d*) Fourier spectrum for the second DOF; and (*e*) phase-plane diagram and (*f*) Fourier spectrum for the third DOF

through the –1 direction along the real axis (Table 2), causing period-2 responses. For period-2 responses of the first and third DOFs, Eq. (21) can be written as

$$x_{10} = \sum_{n=1}^{27} a_{1,(n-1)/2} \cos \frac{(n-1)\tau}{2} + \sum_{n=1}^{26} b_{1,n/2} \sin \frac{n\tau}{2} \tag{62}$$

$$x_{30} = \sum_{n=1}^{27} a_{3,(n-1)/2} \cos \frac{(n-1)\tau}{2} + \sum_{n=1}^{26} b_{3,n/2} \sin \frac{n\tau}{2} \tag{63}$$

One branch of the unstable period-2 response curve is generated at the period-doubling bifurcation points P_9 and P_{10} that are subcritical period-doubling bifurcation points. The stable period-2 response is generated at the period-doubling bifurcation point P_{13}

Table 2 Floquet multipliers for different frequencies near the bifurcation points P_9, P_{10}, and P_{13} on the frequency response curve in Fig. 6(*c*)

	ω	First and second Floquet multipliers λ_1, λ_2	Third and fourth Floquet multipliers λ_3, λ_4	Fifth and sixth Floquet multipliers λ_5, λ_6	Moduli of λ_5, λ_6
Near point P_9	0.75924	$0.13130 \pm 0.58326\bar{i}$	$-0.90688 \pm 0.15820\bar{i}$	–1.01109, –0.67767	1.01109, 0.67767
	0.75974	$0.13010 \pm 0.58358\bar{i}$	$-0.90595 \pm 0.16372\bar{i}$	–0.99704, –0.68774	0.99704, 0.68774
Near point P_{10}	0.84818	$-0.38530 \pm 0.84489\bar{i}$	$0.15097 \pm 0.71912\bar{i}$	–0.93420, –0.56273	0.93420, 0.56273
	0.85171	$-0.35620 \pm 0.85787\bar{i}$	$0.16565 \pm 0.72611\bar{i}$	–1.01805, –0.50528	1.01805, 0.50528
Near point P_{13}	0.90504	$0.08608 \pm 0.92895\bar{i}$	$0.30792 \pm 0.81239\bar{i}$	–0.38332, –1.06180	0.38332, 1.06180
	0.91152	$0.31725 \pm 0.82111\bar{i}$	$0.13728 \pm 0.92324\bar{i}$	–0.90412, –0.44222	0.90412, 0.44222

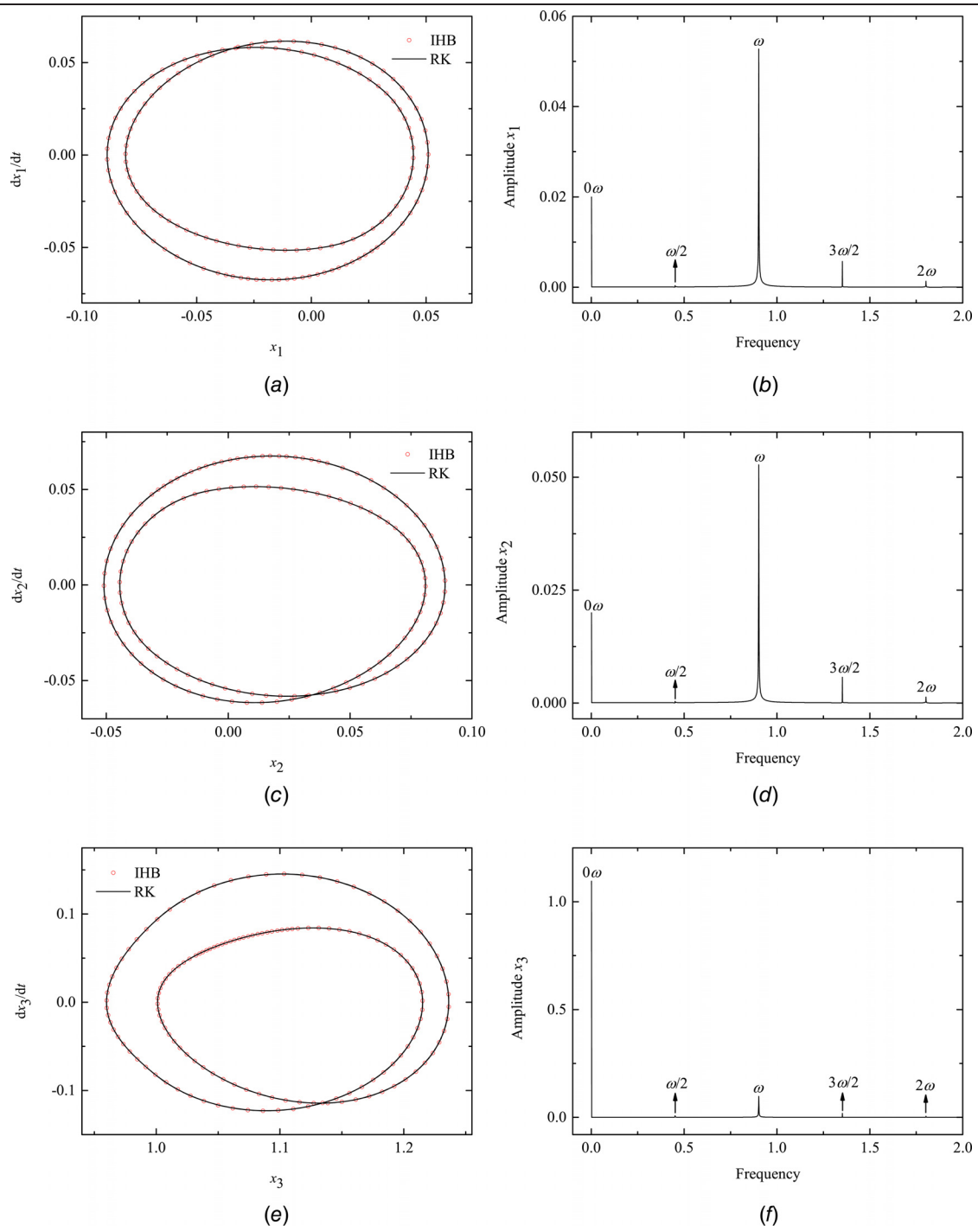

Fig. 8 Period-2 solution as $\omega = 0.90054$ for the three DOFs in Figs. 6(*c*) and 6(*d*): (*a*) phase-plane diagram and (*b*) Fourier spectrum for the first DOF; (*c*) phase-plane diagram and (*d*) Fourier spectrum for the second DOF; and (*e*) phase-plane diagram and (*f*) Fourier spectrum for the third DOF

Table 3 Floquet multipliers for different frequencies near the bifurcation points S_5, P_{17}, and H_4 on the frequency response curve in Fig. 6(*e*)

	ω	First and second Floquet multipliers λ_1, λ_2	Third and fourth Floquet multipliers λ_3, λ_4	Fifth and sixth Floquet multipliers λ_5, λ_6	Moduli of λ_5, λ_6
Near point S_5	1.30659	$-0.88534 \pm 0.22342\bar{i}$	$0.58722 \pm 0.75065\bar{i}$	0.97667, 0.54223	0.97667, 0.54223
	1.30661	$-0.88799 \pm 0.20878\bar{i}$	$0.58716 \pm 0.75070\bar{i}$	1.00323, 0.52891	1.00323, 0.52891
Near point P_{17}	1.48147	$0.48792 \pm 0.61766\bar{i}$	$0.02800 \pm 0.95807\bar{i}$	–1.00086, –0.78416	1.00086, 0.78416
	1.48197	$0.48717 \pm 0.61827\bar{i}$	$0.02646 \pm 0.95812\bar{i}$	–0.99736, –0.78710	0.99736, 0.78710
Near point H_4	1.30804	$-0.22915 \pm 0.87902\bar{i}$	$0.02326 \pm 0.44211\bar{i}$	$0.38532 \pm 0.92084\bar{i}$	0.99821, 0.99821
	1.30754	$-0.22553 \pm 0.87992\bar{i}$	$0.02458 \pm 0.44006\bar{i}$	$0.38687 \pm 0.92472\bar{i}$	1.00239, 1.00239

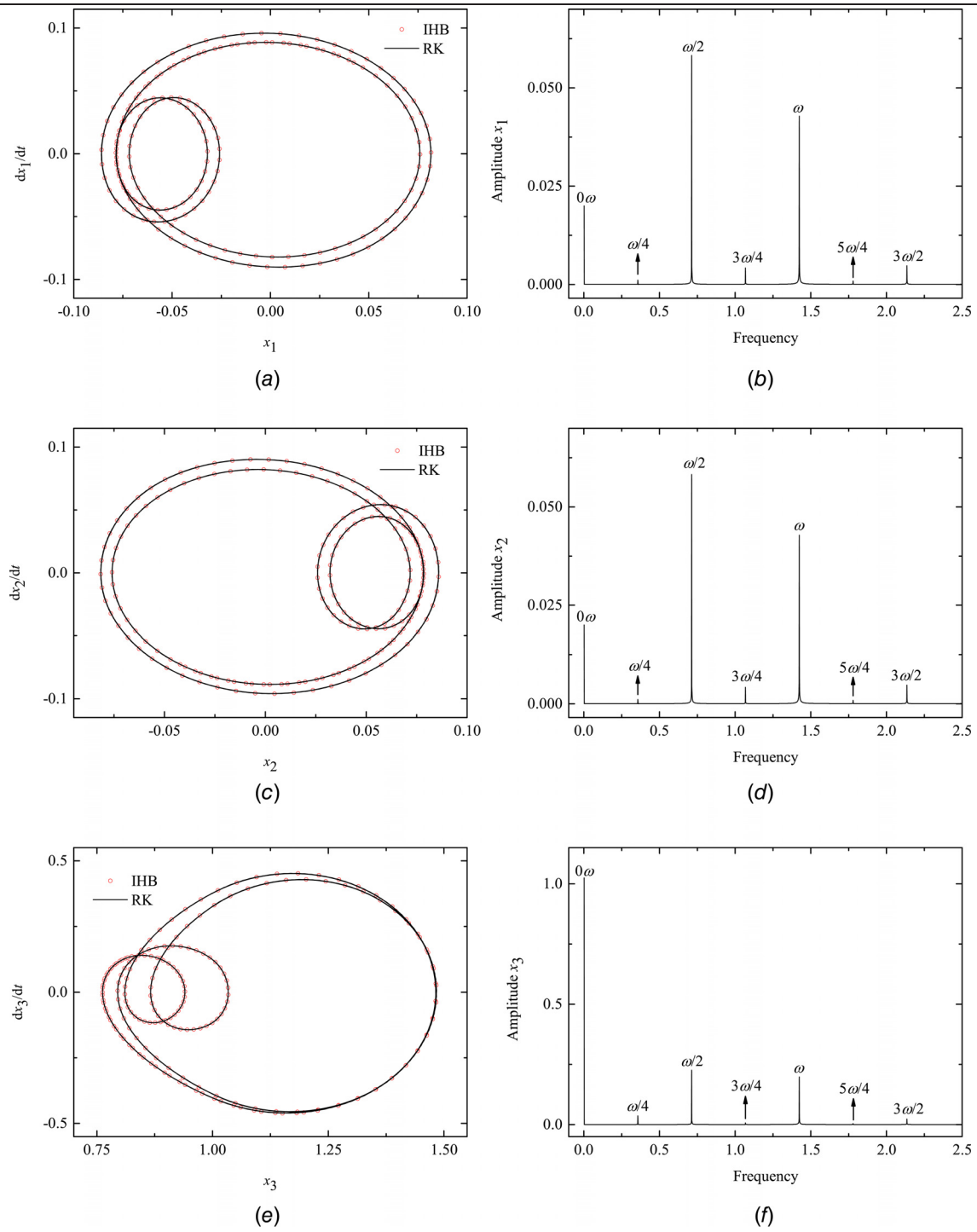

Fig. 9 Period-4 solution as $\omega = 1.42266$ for the three DOFs in Figs. 6(*e*) and 6(*f*): (*a*) phase-plane diagram and (*b*) Fourier spectrum for the first DOF; (*c*) phase-plane diagram and (*d*) Fourier spectrum for the second DOF; and (*e*) phase-plane diagram and (*f*) Fourier spectrum for the third DOF

that is a supercritical period-doubling bifurcation point. In Figs. 6(*c*) and 6(*d*), there are two period-doubling bifurcation points P_{11} and P_{12} and a Hopf bifurcation point H_2 on the period-2 frequency response curve, and a saddle-node bifurcation point S_3 and a period-doubling bifurcation point P_{14} on the period-4 frequency response curve, respectively. On the period-2 frequency response curve, the stable period-4 response curve is generated at the period-doubling bifurcation points P_{11} and P_{12} that are supercritical period-doubling bifurcation points. When the system undergoes the supercritical period-doubling bifurcation points P_{11} and P_{12}, the period-4 solutions are stable in the region from P_{11} to S_3 and P_{12} to P_{14} as moduli of all the Floquet multipliers are less than 1. Figure 8 shows phase-plane diagrams and Fourier spectra of the period-2 response when $\omega = 0.90054$ for the three DOFs in Figs. 6(*c*) and 6(*d*), respectively, where solid lines and circles denote period-2 solutions calculated by utilizing the IHB method and the fourth-order RK method, respectively. As shown in Figs. 8(*a*), 8(*c*), and 8(*e*), the period-2 responses have two cycles and the results of the period-2 solutions obtained from the IHB method coincide with those from numerical integration. Figures 8(*b*), 8(*d*), and 8(*f*) exhibit Fourier spectra of the period-2 response obtained from numerical integration.

In Figs. 6(*e*) and 6(*f*), there exist a saddle-node bifurcation point S_5 and a period-doubling bifurcation point P_{17} on the period-1 frequency response curve. The period-1 solution becomes unstable at the point S_5 as evidenced by a real Floquet multiplier moving away from the unit circle through the $+1$ direction along the real axis (Table 3), resulting in a jump from a stable solution to another stable solution. The period-1 solution loses its stability at the point P_{17} as evidenced by a real Floquet multiplier moving away from the unit circle through the -1 direction along the real axis (Table 3), causing a period-2 response. One can see that the stable period-2 response is generated at the period-doubling bifurcation point P_{17} that is a supercritical period-doubling bifurcation point. Besides, in Figs. 6(*e*) and 6(*f*), there are two period-doubling bifurcation points P_{15} and P_{16}, two Hopf bifurcation points H_3 and H_4, a saddle-node bifurcation point S_4 on the period-2 frequency response curve, and a Hopf bifurcation point H_5 on the period-4 response curve. On the period-2 frequency response curve, a stable period-4 frequency response curve is generated at the period-doubling bifurcation point P_{16} that is a supercritical period-doubling bifurcation point, while the unstable period-4 frequency response curve is destroyed at the period-doubling bifurcation point P_{15} that is a subcritical period-doubling bifurcation point. For the period-4 response, Eq. (21) can be expressed as

$$x_{10} = \sum_{n=1}^{53} a_{1,(n-1)/4} \cos \frac{(n-1)\tau}{4} + \sum_{n=1}^{52} b_{1,n/4} \sin \frac{n\tau}{4} \tag{64}$$

$$x_{30} = \sum_{n=1}^{53} a_{3,(n-1)/4} \cos \frac{(n-1)\tau}{4} + \sum_{n=1}^{52} b_{3,n/4} \sin \frac{n\tau}{4} \tag{65}$$

When the system undergoes the subcritical period-doubling bifurcation point P_{15}, the period-4 response loses its stability in the region from P_{15} to H_5. However, the period-4 response is stable in the region from P_{16} to H_5 as moduli of all the Floquet multipliers are less than 1. Figure 9 exhibits phase-plane diagrams and Fourier spectra of the period-4 response when $\omega = 1.42266$ for the three DOFs in Figs. 6(*e*) and 6(*f*), where solid lines and circles denote the period-4 solutions calculated by utilizing the IHB method and the fourth-order RK method, respectively. As shown in Figs. 9(*a*), 9(*c*), and 9(*e*), the period-4 responses have four cycles and the results of the period-4 solutions obtained from the IHB method agree very well with those from numerical integration. Figures 9(*b*), 9(*d*), and 9(*f*) exhibit Fourier spectra of the period-4 response obtained from numerical integration.

6 Conclusions

Various bifurcation phenomena and period-doubling responses in a gear transmission system with multipiecewise linear functions under internal and external excitations are discussed in detail in this work. The IHB method is employed on a three-DOF model of the gear transmission system to work out periodic and period-doubling responses of the three-DOF model, in which three piecewise linear functions caused by gear backlashes and radial clearances in bearings are taken into account. An improved Floquet theory is formulated for the system with multipiecewise linear functions by considering the precise Hsu's method and piecewise linear functions. Stability of periodic and period-doubling solutions and types of bifurcation points on frequency response curves of the gear transmission system are accurately analyzed by utilizing the Floquet theory. Various nonlinear phenomena that exist in frequency response curves are discussed. Features of periodic and period-doubling responses are characterized by phase-plane diagrams and Fourier spectra. The periodic and period-doubling solutions obtained by the IHB method agree very well with those obtained through the fourth-order RK method.

Under internal and external excitations, softening-spring behaviors characterized by frequency response curves bending to the left, and primary, superharmonic, and subharmonic resonances are observed on frequency response curves. Three types of bifurcations that contain saddle-node, period-doubling, and Hopf bifurcations are observed. The jump phenomenon from a stable periodic solution to another stable periodic solution generated by a saddle-node bifurcation and period-doubling responses produced by a period-doubling bifurcation are observed. The above summary indicates that there exist abundant and interesting nonlinear phenomena in the gear transmission system.

Funding Data

- National Natural Science Foundation of China (Grant Nos. 11972381 and 11772100; Funder ID: 10.13039/501100001809).
- Guangdong Basic and Applied Basic Research Foundation (Grant No. 2022A1515011809; Funder ID: 10.13039/501100007162).

References

[1] Wang, J. J., Li, R. F., and Peng, X. H., 2003, "Survey of Nonlinear Vibration of Gear Transmission Systems," ASME Appl. Mech. Rev., **56**(3), pp. 309–329.
[2] Liang, X. H., Zuo, M. J., and Feng, Z. P., 2018, "Dynamic Modeling of Gearbox Faults: A Review," Mech. Syst. Signal Process., **98**, pp. 852–876.
[3] Cooley, C. G., and Parker, R. G., 2014, "A Review of Planetary and Epicyclic Gear Dynamics and Vibrations Research," ASME Appl. Mech. Rev., **66**(4), p. 040804.
[4] Sheng, L., Li, W., Wang, Y., Fan, M., and Yang, X., 2019, "Nonlinear Dynamic Analysis and Chaos Control of Multi-Freedom Semi-Direct Gear Drive System in Coal Cutters," Mech. Syst. Signal Process., **116**, pp. 62–77.
[5] Li, Z. X., and Peng, Z., 2016, "Nonlinear Dynamic Response of a Multi-Degree of Freedom Gear System Dynamic Model Coupled With Tooth Surface Characters: A Case Study on Coal Cutters," Nonlinear Dyn., **84**(1), pp. 271–286.
[6] Li, Z., Zhu, C., Liu, H., and Gu, Z., 2020, "Mesh Stiffness and Nonlinear Dynamic Response of a Spur Gear Pair Considering Tribo-Dynamic Effect," Mech. Mach. Theory, **153**, p. 103989.
[7] Li, S., and Kahraman, A., 2013, "A Tribo-Dynamic Model of a Spur Gear Pair," J. Sound Vib., **332**(20), pp. 4963–4978.
[8] Jiang, Y., Zhu, H., Li, Z., and Peng, Z., 2016, "The Nonlinear Dynamics Response of Cracked Gear System in a Coal Cutter Taking Environmental Multi-Frequency Excitation Forces Into Consideration," Nonlinear Dyn., **84**(1), pp. 203–222.
[9] Chen, Z., Ning, J., Wang, K., and Zhai, W., 2021, "An Improved Dynamic Model of Spur Gear Transmission Considering Coupling Effect Between Gear Neighboring Teeth," Nonlinear Dyn., **106**(1), pp. 339–357.
[10] Litak, G., and Friswell, M. I., 2005, "Dynamics of a Gear System With Faults in Meshing Stiffness," Nonlinear Dyn., **41**(4), pp. 415–421.
[11] Parker, R. G., Vijayakar, S. M., and Imajo, T., 2000, "Non-Linear Dynamic Response of a Spur Gear Pair: Modelling and Experimental Comparison," J. Sound Vib., **237**(3), pp. 435–455.
[12] Dong, J., Wang, S., Lin, H., and Wang, Y., 2016, "Dynamic Modeling of Double-Helical Gear With Timoshenko Beam Theory and Experiment Verification," Adv. Mech. Eng., **8**(5), pp. 1–14.
[13] Theodossiades, S., and Natsiavas, S., 2000, "Non-Linear Dynamics of Gear-Pair System With Periodic Stiffness and Backlash," J. Sound Vib., **229**(2), pp. 287–310.

[14] Moradi, H., and Salarieh, H., 2012, "Analysis of Nonlinear Oscillations in Spur Gear Pairs With Approximated Modelling of Backlash Nonlinearity," Mech. Mach. Theory, **51**, pp. 14–31.
[15] Guo, Y., and Parker, R. G., 2012, "Dynamic Analysis of Planetary Gears With Bearing Clearance," ASME J. Comput. Nonlinear Dyn., **7**(4), p. 041002.
[16] Kahraman, A., and Singh, R., 1990, "Non-Linear Dynamics of a Spur Gear Pair," J. Sound Vib., **142**(1), pp. 49–75.
[17] Cao, Z., Chen, Z. G., and Jiang, H. J., 2020, "Nonlinear Dynamics of a Spur Gear Pair With Force-Dependent Mesh Stiffness," Nonlinear Dyn., **99**(2), pp. 1227–1241.
[18] Guilbault, R., Lalonde, S., and Thomas, M., 2012, "Nonlinear Damping Calculation in Cylindrical Gear Dynamic Modeling," J. Sound Vib., **331**(9), pp. 2110–2128.
[19] Mo, S., Zhang, Y., Song, Y., Song, W., and Huang, Y., 2022, "Nonlinear Vibration and Primary Resonance Analysis of Non-Orthogonal Face Gear-Rotor-Bearing System," Nonlinear Dyn., **108**(4), pp. 3367–3389.
[20] Sun, Z., Chen, S., Hu, Z., and Lei, D., 2022, "Vibration Response Analysis of a Gear-Rotor-Bearing System Considering Steady-State Temperature," Nonlinear Dyn., **107**(1), pp. 477–493.
[21] Wang, S., and Zhu, R., 2021, "Nonlinear Dynamic Analysis of GTF Gearbox Under Friction Excitation With Vibration Characteristics Recognition and Control in Frequency Domain," Mech. Syst. Signal Process., **151**, p. 107373.
[22] Lin, C., Wang, Y., Hu, Y., Ran, G., and Yu, Y., 2022, "Nonlinear Dynamic Analysis of Eccentric Curve-Face Gear Transmission System," J. Sound Vib., **520**, p. 116596.
[23] Zhang, Q., Wang, X., Wu, S., Cheng, S., and Xie, F., 2022, "Nonlinear Characteristics of a Multi-Degree-of-Freedom Wind Turbine's Gear Transmission System Involving Friction," Nonlinear Dyn., **107**(4), pp. 3313–3338.
[24] Lau, S. L., and Cheung, Y. K., 1981, "Amplitude Incremental Variational Principle for Nonlinear Vibration of Elastic Systems," ASME J. Appl. Mech., **48**(4), pp. 959–964.
[25] Cheung, Y. K., and Lau, S. L., 1982, "Incremental Timespace Finite Strip Method for Non-Linear Structural Vibrations," Earthquake Eng. Struct. Dyn., **10**(2), pp. 239–253.
[26] Lau, S. L., Cheung, Y. K., and Wu, S. Y., 1982, "A Variable Parameter Incrementation Method for Dynamic Instability of Linear and Nonlinear Elastic Systems," ASME J. Appl. Mech., **49**(4), pp. 849–853.
[27] Lau, S. L., and Zhang, W.-S., 1992, "Nonlinear Vibrations of Piecewise-Linear Systems by Incremental Harmonic Balance Method," ASME J. Appl. Mech., **59**(1), pp. 153–160.
[28] Shen, Y. J., Yang, S. P., and Liu, X. D., 2006, "Nonlinear Dynamics of a Spur Gear Pair With Time-Varying Stiffness and Backlash Based on Incremental Harmonic Balance Method," Int. J. Mech. Sci., **48**(11), pp. 1256–1263.
[29] Kahraman, A., and Singh, R., 1991, "Non-Linear Dynamics of a Geared Rotor-Bearing System With Multiple Clearances," J. Sound Vib., **144**(3), pp. 469–506.
[30] Kahraman, A., and Blankenship, G., 1996, "Interactions Between Commensurate Parametric and Forcing Excitations in a System With Clearence," J. Sound Vib., **194**(3), pp. 317–336.
[31] Choi, Y., and Noah, S., 1988, "Forced Periodic Vibration of Unsymmetric Piecewise-Linear Systems," J. Sound Vib., **121**(1), pp. 117–126.
[32] Zhou, S., Song, G., Li, Y., Huang, Z., and Ren, Z., 2019, "Dynamic and Steady Analysis of a 2-DOF Vehicle System by Modified Incremental Harmonic Balance Method," Nonlinear Dyn., **98**(1), pp. 75–94.
[33] Vorotnikov, K., and Starosvetsky, Y., 2016, "Bifurcation Structure of the Special Class of Nonstationary Regimes Emerging in the 2D Inertially Coupled, Unit-Cell Model: Analytical Study," J. Sound Vib., **377**, pp. 226–242.
[34] Cheung, Y. L., Chen, S. H., and Lau, S. L., 1990, "Application of the Incremental Harmonic Balance Method to Cubic Non-Linearity Systems," J. Sound Vib., **140**(2), pp. 273–286.
[35] Huang, J. L., Xiao, L. J., and Zhu, W. D., 2020, "Investigation of Quasi-Periodic Response of a Buckled Beam Under Harmonic Base Excitation With an "Unexplained" Sideband Structure," Nonlinear Dyn., **100**(3), pp. 2103–2119.
[36] Hsu, C. S., and Cheng, W.-H., 1973, "Applications of the Theory of Impulsive Parametric Excitation and New Treatments of General Parametric Excitation Problems," ASME J. Appl. Mech., **40**(1), pp. 78–86.
[37] Hsu, C. S., 1972, "Impulsive Parametric Excitation: Theory," ASME J. Appl. Mech., **39**(2), pp. 551–558.
[38] Huang, J. L., Su, R. K. L., and Chen, S. H., 2009, "Precise Hsu's Method for Analyzing the Stability of Periodic Solutions of Multi-Degrees-of-Freedom Systems With Cubic Nonlinearity," Comput. Struct., **87**(23–24), pp. 1624–1630.
[39] Nayfeh, A. H., and Balachandran, B., 1995, *Applied Nonlinear Dynamics: Analytical, Computational, and Experimental Methods*, Wiley, New York.
[40] Huang, J. L., Su, R. K. L., Lee, R. Y. Y., and Chen, S. H., 2018, "Various Bifurcation Phenomena in a Nonlinear Curved Beam Subjected to Base Harmonic Excitation," Int. J. Bifurcation Chaos, **28**(07), p. 1830023.